

Pressured-induced superconductivity extending across the topological phase transition in thallium-based topological materials $\text{TlBi}(\text{S}_{1-x}\text{Se}_x)_2$

Cuiying Pei^{1,12}, Peihao Huang^{2,3,12}, Peng Zhu^{4,5,6,12}, Linlin Liu^{2,3,12}, Qi Wang^{1,7}, Yi Zhao¹, Lingling Gao¹, Changhua Li¹, Weizheng Cao¹, Jian Lv^{2,3}, Xiang Li^{4,5,6}, Zhiwei Wang^{4,5,6*}, Yugui Yao^{4,5}, Binghai Yan^{8*}, Claudia Felser⁹, Yulin Chen^{1,7,10}, Hanyu Liu^{2,3*}, Yanpeng Qi^{1,7,11,13*}

¹ School of Physical Science and Technology, ShanghaiTech University, Shanghai 201210, China

² State Key Laboratory of Superhard Materials and International Center for Computational Method and Software, College of Physics, Jilin University, Changchun 130012, China

³ International Center of Future Science, Jilin University, Changchun 130012, China

⁴ Centre for Quantum Physics, Key Laboratory of Advanced Optoelectronic Quantum Architecture and Measurement (MOE), School of Physics, Beijing Institute of Technology, Beijing 100081, China

⁵ Beijing Key Lab of Nanophotonics and Ultrafine Optoelectronic Systems, Beijing Institute of Technology, Beijing 100081, China

⁶ Material Science Center, Yangtze Delta Region Academy of Beijing Institute of Technology, Jiaxing, 314011, P. R. China

⁷ ShanghaiTech Laboratory for Topological Physics, ShanghaiTech University, Shanghai 201210, China

⁸ Department of Condensed Matter Physics, Weizmann Institute of Science, Rehovot 7610001, Israel

⁹ Max Planck Institute for Chemical Physics of Solids, Dresden 01187, Germany

¹⁰ Department of Physics, Clarendon Laboratory, University of Oxford, Parks Road, Oxford OX1 3PU, UK

¹¹ Shanghai Key Laboratory of High-resolution Electron Microscopy, ShanghaiTech University, Shanghai 201210, China

¹² These authors contributed equally

* Corresponding author's email address: Y.Q. (qiyp@shanghaitech.edu.cn) or H.L. (lhy@calypso.cn) or B.Y. (binghai.yan@weizmann.ac.il) or Z.W. (zhiweiwang@bit.edu.cn)

SUMMARY

The coexistence of superconductivity and topology holds the potential to realize exotic quantum states of matter. Here we report that superconductivity induced by high pressure in three thallium-based materials, covering the phase transition from a normal insulator (TlBiS_2) to a topological insulator (TlBiSe_2) through a Dirac semimetal (TlBiSeS). By increasing the pressure up to 60 GPa, we observe superconductivity phase diagrams with maximal T_c values at 6.0~8.1 K. Our density-functional theory calculations reveal topological surface states in superconductivity phases for all three compounds. Our study paves the path to explore topological superconductivity and topological phase transitions.

¹³ Lead Contact's email address: Yanpeng Qi (qiyp@shanghaitech.edu.cn)

INTRODUCTION

The discovery of topological states and topological phase transitions has reshaped our understanding of physics and materials over the past few years.^[1; 15; 28; 40; 41; 56; 58] The topological transition from a normal insulator to a topological insulator (TI) can be realized by chemical or mechanical pressure. The topological transition was first predicted^[59] and demonstrated^[44; 57] in TI-based chalcogenides $\text{TlBi}(\text{S}_{1-x}\text{Se}_x)_2$ by increasing the Se component. The chemical pressure increases the amplitude of the spin-orbit coupling (SOC) with the critical transition point at $x = 0.5$, that is, TlBiSSe , which is a 3D Dirac semimetal.^[5; 23; 24; 30; 38; 43; 46] Instead, mechanical pressure pushes the bandgap of a normal insulator to close and re-open, leading to a nontrivial topological state. Furthermore, superconductivity may emerge with pressure and interplay with topological surface states, leading to possible topological superconductivity on the surface by the self-proximity effect.^[8]

In this study, we apply hydrostatic pressure to $\text{TlBi}(\text{S}_{1-x}\text{Se}_x)_2$ and investigate the effects of chemical and mechanical pressures on the phase transition and induced superconductivity, as shown in **Figure 1**. Maximum critical temperatures, T_c , of 8.1, 7.0 and 6.0 K are observed for TlBiS_2 , TlBiSeS and TlBiSe_2 , respectively. Our theoretical calculations demonstrate the coexistence of topological features and superconductivity in $\text{TlBi}(\text{S}_{1-x}\text{Se}_x)_2$ ($x = 0, 0.5$ and 1) upon compression.

RESULTS AND DISCUSSION

Crystal structure of $\text{TlBi}(\text{S}_{1-x}\text{Se}_x)_2$ ($x = 0, 0.5, 1$) in ambient condition

The $\text{TlBi}(\text{S}_{1-x}\text{Se}_x)_2$ ($x = 0, 0.5, 1$) single crystals used in this study were grown using the melting method. All samples form a rhombohedral crystal structure with the space group $R\bar{3}m$, which possesses real-space-inversion symmetry and can be viewed as a distorted NaCl structure with four atoms in the primitive unit cell. The stacking sequence of each layer is -Tl-X-Bi-X- along the $[111]$ direction, and the binding between the layers is rather strong, in contrast to the van der Waals type coupling of tetradymite semiconductors. The high crystallinity and homogeneity of our single

crystals were confirmed by X-ray diffraction (XRD) and energy dispersive X-ray spectroscopy (EDS) analysis (Figure S1).

Structural phase transition of $\text{TlBi}(\text{S}_{1-x}\text{Se}_x)_2$ ($x = 0, 0.5, 1$) under high pressure

Before the physical property measurements, we investigated the pressure-induced structural evolution of $\text{TlBi}(\text{S}_{1-x}\text{Se}_x)_2$ ($x = 0, 0.5, 1$) using XRD with a wavelength of $\lambda = 0.6199 \text{ \AA}$. Figure 2a shows a typical XRD pattern of TlBiSeS up to 40.6 GPa. Two structural phase transitions were observed under high pressure. All the diffraction peaks at 1 atm can be indexed well to a rhombohedral $R\bar{3}m$ structure by Rietveld refinement with lattice parameters of $a = 4.205(2) \text{ \AA}$ and $c = 21.734(1) \text{ \AA}$ (Figure S2a and Table S1). There was no obvious spectral change below 8.6 GPa. At 8.6 GPa, additional diffraction peaks marked by asterisks emerged, signifying the formation of phase II. When the pressure reaches 19.3 GPa, phase II began to transition into a new phase III. Above 26.6 GPa, the transformation is complete and no further transitions are observed up to 40.6 GPa. Pressure-dependent Raman spectroscopy of TlBiSeS (Figure 2c) further demonstrated the crystallographic structural phase transition sequence under high pressure, which is consistent with *in-situ* XRD results.

To identify the crystal structures of TlBiSeS under high pressure, we performed an additional structure prediction for this system using our developed structure prediction methodology.^[10; 50; 51] As a result of extensive simulations, our structure searches successfully reproduced the experimental $R\bar{3}m$ structure (Phase I) at ambient pressure, validating our computational scheme. Our computed enthalpy difference curves for the predicted phases, as shown in Figure S2, indicate a phase transition at 9.1 GPa, where Phase II (space group $C2/m$ structure, No. 12) demonstrates a lower enthalpy than that of phase I ($R\bar{3}m$ structure). As the pressure is higher than 21.3 GPa, another newly predicted phase (Phase III, space group $P4mm$, No. 99) is energetic and stable. The experimental structural phase transition coincided with the theoretical prediction. In addition, the phonon dispersion curves were used to study the dynamic structural stability of the predicted structure. As shown in Figure S3, no imaginary frequency was found for these two structures, indicating their dynamic stability.

The observed XRD data were then refined using the predicted structures. Figure S4b and S4c show the typical Rietveld refinement results for TlBiSeS at various pressures. The excellent Rietveld fitting of the predicted structures makes the determination of the high-pressure phases unambiguous. Phase II possesses a monoclinic structure, whereas phase III crystals are in a tetragonal phase. Figure 2b shows the volume data as a function of pressure for the different phases. The two-phase transitions are characterized by first orders accompanying 2.4 and 4.4% volume collapse at the transitions. A similar structural evolution under pressure was observed for TlBiS₂ and TlBiSe₂ (Figure S5).

To gain insight into the structural evolution, pressure-induced coordination of Tl and Bi was derived from the Rietveld refinements, as shown in Figure 2d. In ambient condition, TlBiSeS exhibits inversion symmetry, where both Tl and Bi act as inversion centers.^[60] Continuous bonding was found perpendicular to the layers, and octahedral TlSe(S)₆ and BiSe(S)₆ coupling interlayers led to an essentially three-dimensional crystal structure.^[4] Although the stacking order is similar between phase I and phase II, there are seven Se(S) atoms as ligands in phase II, in contrast to the six-coordinated phase I. In phase III, Tl and Bi atoms are centered in the cuboid ($a = b \neq c$) to form eight-fold bonding with Se(S). The TlSe(S)₈ cuboid and BiSe(S)₈ cuboid are face shared and sandwiched along the *c*-axis.

Pressure-induced superconductivity in TlBi(S_{1-x}Se_x)₂ ($x = 0, 0.5, 1$)

At ambient pressure, TlBiSeS exhibited metallic-like behavior and electron-type charge carriers with a concentration of $n_e \sim 1.94 \times 10^{18} \text{ cm}^{-3}$ at 300 K (Figure S6), which is close to previously reported values.^[31] Since TlBiSeS exhibits multi-phase transitions under high pressure, a question arises naturally: what will happen for transport properties? Hence, we measured the electrical resistivity $\rho(T)$ of the TlBiSeS single crystals at various pressures. Figure 3 shows the typical $\rho(T)$ curves of TlBiSeS for pressures up to 54.6 GPa. The resistivity of TlBiSeS first increases with applied pressure and reaches the maximum value at 6.3 GPa. TlBiSeS shows insulator or

semiconducting-like behavior at this pressure region. Upon further increasing the pressure, resistivity starts to decrease rapidly, and a metal-insulator transition occurs. Superconductivity appears with pressure increases, and a maximum T_c of 6.7 K is attained at $P = 19.9$ GPa (Figure 3). Beyond this pressure, T_c decreases slowly, but superconductivity persists up to the highest experimental pressure of ~ 55 GPa. The appearance of superconductivity in TlBiSeS is further corroborated by the resistivity data in applied magnetic fields. As shown in Figure 3e, the superconducting transition gradually shifts toward lower temperatures with increasing magnetic fields. The value of $\mu_0 H_{c2}(T)$ was estimated to be 2.86 T at 23.3 GPa (Figure 3f), which yields a Ginzburg–Landau coherence length $\xi_{GL}(0)$ of 10.74 nm. In analogy with that of TlBiSeS, pressure-induced superconductivity with a maximum T_c of 8.1 K and 6.0 K is observed in TlBiS₂ and TlBiSe₂, respectively. The values of T_c shown here are quite higher than that in TlBiTe₂.^[16] Temperature dependence of the upper critical field for TlBiS₂ at 22.7 GPa and TlBiSe₂ at 16.3 GPa are also shown in Figure 3f.

T-P phase diagram of TlBi(S_{1-x}Se_x)₂ ($x = 0, 0.5, 1$)

High-pressure transport measurements on TlBi(S_{1-x}Se_x)₂ ($x = 0, 0.5, 1$) single crystals for several independent runs provided consistent and reproducible results (Figures S7-S16), confirming the intrinsic superconductivity under pressure. Based on the above resistivity, XRD, and Raman measurements, the T - P phase diagram is summarized in Figure 4. These results demonstrate that high pressure dramatically alters both crystal and electronic structures of TlBiS₂, TlBiSeS, and TlBiSe₂. In phase I, the resistivity of TlBiS₂ exhibited a non-monotonic evolution with increasing pressure. Over the entire temperature range, the resistivity is first suppressed with the applied pressure and reaches a minimum value at approximately 4.1 GPa. With a further increase in pressure, the resistivity increases again, and a transition from metallic to semiconducting behavior occurs. This peculiar behavior of resistivity is not associated with a structural phase transition because high-pressure XRD studies revealed structural stability in this pressure range. Our high-pressure Raman results indicated a clear anomaly in the phonon linewidths of E_g mode at pressures ~ 2.8 GPa, which is

consistent with the pressure of the minimum resistivity (Figure S17). This anomaly is evidence of topological phase transitions. A similar phenomenon was observed for black phosphorus^[12], Sb₂Te₃^[11], and BiTeI^[39]. A dome-shaped evolution of electrical resistivity with pressure was observed in TlBiSeS; however, the resistivity of TlBiSe₂ exhibited a monotonic decrease with increasing pressure. In phase II, our band structure calculations demonstrate that both TlBiS₂ and TlBiSeS are normal semiconductors with narrow bandgaps ($\Delta E \sim 238$ meV and 85 meV for TlBiS₂ and TlBiSeS, respectively), whereas TlBiSe₂ is a semimetal without a global bandgap, in agreement with our resistivity results (Figure S18). The resistivity abruptly decreased and ultimately underwent metallization in this pressure range. It should be noted that a small drop of ρ is observed, and no zero resistivity is achieved in this pressure region, probably because of the small amount of phase III. In phase III, the resistivity of all three samples did not change significantly in response to further increases in the pressure. Superconductivity was observed in this region, and the T_c values of all three samples decreased monotonically with increasing pressure. The observed superconductivity in the high-pressure range is associated with structural instability and/or pressure-induced structural phase transition. The evolution of superconductivity is probably due to a reduction of density of state at the Fermi level.^[19; 32]

Pressure-induced topological properties evolution on TlBi(S_{1-x}Se_x)₂ (x = 0, 0.5, 1)

Because superconductivity was observed in Phase III, we performed detailed *ab initio* calculations to identify the topological nature of TlBiSeS at 30 GPa. As shown in Figure 5, there is an SOC-induced band inversion near the Fermi surface at the Γ and X points. The inverted bandgaps were approximately 688 and 662 meV, respectively. We confirmed the non-trivial topological character by calculating the Z₂ topological invariant, parity eigenvalues (Table S2). Wannier charge center (Figure S19) and topological edge states (Figure 5c) of TlBiSeS at 30 GPa^[7; 9]. The inherent metallicity of TlBiSeS at 30 GPa can be easily identified by their bands crossing at the Fermi level, which are consistent with their Fermi surfaces shown in Figure 5d. Thus, TlBiSeS at 30 GPa can be interpreted as a non-trivial topological metal. Superconducting

transitions in this phase are supported by their intrinsic metallic features. The Dirac-cone-like surface states of TlBiSeS at 30 GPa are located at 0.19 eV above Fermi level, inside the SOC gap between the bulk valence band and the bulk conduction band. We also performed theoretical calculations for TlBiS₂ and TlBiSe₂, and all samples showed nontrivial band structures in phase III (Figures S20-S22). Therefore, the combined theoretical calculations and *in-situ* high pressure measurements demonstrate the coexistence of topological feature and superconductivity in TlBi(S_{1-x}Se_x)₂ ($x = 0, 0.5$, and 1) upon compression. Our study will stimulate further studies, such as the 4π -periodic Josephson effect^[25; 54] and quantum oscillations under high pressure^[2; 6], to investigate topological superconductivity and help the exploration of Majorana fermions.

We discovered pressure-induced superconductivity in thallium-based III-V-IV₂ ternary chalcogenides TlBi(S_{1-x}Se_x)₂ ($x = 0, 0.5, 1$) topological materials by combining experimental and theoretical investigations. High pressure dramatically alters the electronic state, and superconductivity is observed in all three samples after the two structural phase transitions. Theoretical calculations indicated that TlBi(S_{1-x}Se_x)₂ ($x = 0, 0.5, 1$) with a tetragonal $P4mm$ structure is considered as a topological metal, which coexists with superconductivity. Our results demonstrate that TlBi(S_{1-x}Se_x)₂ compounds with a nontrivial topology of electronic states display new ground states upon compression and have potential applications in next-generation spintronic devices.

EXPERIMENTAL PROCEDURES

Resource availability

Lead Contact

Further information and requests for the samples should be directed to and will be fulfilled by the Lead Contact, Yanpeng Qi (qiyp@shanghaitech.edu.cn).

Materials Availability

All the samples used in this study are available from the Lead Contact without restriction.

Data and Code Availability

All relevant data are available from the corresponding author upon reasonable request.

Sample Preparation

Single crystals of $\text{TlBi}(\text{S}_{1-x}\text{Se}_x)_2$ ($x = 0, 0.5, 1$) were grown by a melting method starting from high purity (more than 4N) of elementary Tl, Bi, Se and S shots sealed in an evacuated quartz tube. In order to obtain crystals with high-quality, we performed surface cleaning for all starting materials except S, to remove the oxide layers formed in air.^[52; 53] The elements were heated to 800 °C in several hours and kept for 48 h, at which the tubes were intermittently shaken to ensure homogeneity of the melt; after that, they were slowly cooled down to 400 °C in 100 h and subsequently down to room temperature with the furnace switched off.

High-pressure Measurements

Nonmagnetic diamond anvil cell (DAC) was employed to perform the *in situ* high-pressure resistivity measurements as described elsewhere.^[3; 34-36; 42] A cubic BN/epoxy mixture was used as insulating layer between BeCu gaskets and electrical leads. Four Pt foils were arranged in a van der Pauw four-probe configuration to contact the sample in the chamber for resistivity measurements. Pressure was determined by the ruby luminescence method.^[27] The *in situ* high-pressure Raman spectroscopy measurements were performed using a Raman spectrometer (Renishaw inVia, U.K.) with a laser excitation wavelength of 532 nm and low-wavenumber filter. Symmetric DAC with anvil culet sizes of 300 μm was used, with silicon oil as pressure transmitting medium (PTM). *In situ* high-pressure synchrotron x-ray diffraction (XRD) measurements were carried out at room temperature with sample powder grinded from single crystals at the beamline BL15U of Shanghai Synchrotron Radiation Facility (X-ray wavelength $\lambda = 0.6199 \text{ \AA}$). Symmetric DACs with anvil culet sizes of 300 μm and T301 gaskets were used. Silicon oil was used as the PTM and pressure was determined by the ruby luminescence method.^[27] The 2D diffraction patterns were analyzed using the FIT2D software.^[14] General Structure Analysis System (GSAS) and the graphical user interface EXPGUI^[26; 47] were employed for Rietveld refinements on crystal structures under high pressure.

Theoretical Calculation

A swam-intelligence-based CALYPSO method and its same-name code^[10; 50; 51] was used to predict structure. VASP plane-wave code^[20; 21] was employed to calculate Density functional total energy and structure relaxation. Perdew-Burke-Ernzerhof (PBE) generalized gradient approximation density functional^[37] and frozen-core all-electron projector-augmented wave (PAW) potentials^[22] was adopted in our calculations. The electronic wave functions are expanded in a plane-wave basis set with a kinetic energy cutoff of 400 eV. The Brillouin zone (BZ) are sampled with a k-meshes with a reciprocal space resolution of $2\pi \times 0.03 \text{ \AA}^{-1}$ and energies are converged to 1 meV/atom. Supercell approach^[33] as implemented in the Phonopy code^[48] were used to calculate phonon spectrum. Heyd-Scuseria-Ernzerhof (HSE06) Hybrid functional implemented in PWmat^[17; 18] to improve the accuracy of the band gap. It runs on graphics processing unit (GPU) processors. The NCPP-SG15-PBE^[13; 45] pseudopotential is used as well. Using an energy cutoff of 50 Ry, the convergence threshold of the total energy is less than 10^{-4} eV. The Brillouin zone sampling is performed on Monkhorst–Pack scheme on 4*6*9 special k-points for structure optimization and electronic structural calculations. The maximally localized Wannier functions were constructed from DFT by the WANNIER90^[29] code and then used to calculate the Wannier charge center, the Z2 topological invariant, and edge states. Based on tight-binding parameters from Wannier90^[29], WannierTools^[55] provides post-processing analysis. Band topologies were calculated using vasp2trace code^[49].

SUPPLEMENTAL INFORMATION

Supplemental information can be found online.

ACKNOWLEDGMENTS

C. Pei, P. Huang, P. Zhu and L. Liu contributed equally to this work. We thank Prof. Yanming Ma for valuable discussions. This work was supported by the National Key

R&D Program of China (Grant No. 2018YFA0704300, 2020YFA0308800), the National Natural Science Foundation of China (Grant No. U1932217, 11974246, 12004252, 92065109 and 12074138), the Science and Technology Commission of Shanghai Municipality (19JC1413900) and Shanghai Science and Technology Plan (Grant No. 21DZ2260400). The authors thank the support from Analytical Instrumentation Center (SPST-AIC10112914) and Centre for High resolution Electron Microscopy (*ChEM*) (No. EM02161943), SPST, ShanghaiTech University. The authors thank the staffs from BL15U1 at Shanghai Synchrotron Radiation Facility for assistance during data collection. B.Y. acknowledges the financial support by the European Research Council (ERC Consolidator Grant "NonlinearTopo", No. 815869) and the ISF - Quantum Science and Technology (No. 1251/19). Z.W. thanks the Analysis & Testing Center at BIT for assistance in facility support.

AUTHOR CONTRIBUTIONS

Y.P.Q. designed research; C.Y.P., P.Z., Q.W., Y.Z., L.L.G., C.H.L., W.Z.C., X.L. performed experiments; P.H.H., L.L.L., J.L. carried out theoretical calculations; Y.P.Q., H.Y.L., B.H.Y., Z.W.W., C.Y.P., P.H.H, L.L.L., Y.G.Y., C.F. and Y.L.C. analyzed data and wrote the paper.

DECLARATION OF INTERESTS

The authors declare no competing interests.

REFERENCES

- [1] Ando, Y. (2013). Topological Insulator Materials. *J Phys Soc Jpn* 82, 102001. 10.7566/jpsj.82.102001.
- [2] Cai, P.L., Hu, J., He, L.P., Pan, J., Hong, X.C., Zhang, Z., Zhang, J., Wei, J., Mao, Z.Q., and Li, S.Y. (2015). Drastic pressure effect on the extremely large magnetoresistance in WTe₂: quantum oscillation study. *Phys Rev Lett* 115, 057202. 10.1103/PhysRevLett.115.057202.
- [3] Cao, W., Zhao, N., Pei, C., Wang, Q., Zhao, Y., Gao, L., Li, C., Yu, N., Chen, Y., Liu, K., *et al.* (2021). pressure induced superconductivity in noncentrosymmetric Weyl semimetals LaAlX (X = Si, Ge). arXiv:2111.02882.
- [4] Cava, R.J., Ji, H., Fuccillo, M.K., Gibson, Q.D., and Hor, Y.S. (2013). Crystal

- structure and chemistry of topological insulators. *J Mater Chem C* *1*, 3176. 10.1039/c3tc30186a.
- [5] Chen, Y.L., Liu, Z.K., Analytis, J.G., Chu, J.H., Zhang, H.J., Yan, B.H., Mo, S.K., Moore, R.G., Lu, D.H., Fisher, I.R., *et al.* (2010). Single Dirac cone topological surface state and unusual thermoelectric property of compounds from a new topological insulator family. *Phys Rev Lett* *105*, 266401. 10.1103/PhysRevLett.105.266401.
- [6] dos Reis, R.D., Wu, S.C., Sun, Y., Ajeesh, M.O., Shekhar, C., Schmidt, M., Felser, C., Yan, B., and Nicklas, M. (2016). Pressure tuning the Fermi surface topology of the Weyl semimetal NbP. *Phys Rev B* *93*, 205102. 10.1103/PhysRevB.93.205102.
- [7] Fu, L., and Kane, C.L. (2007). Topological insulators with inversion symmetry. *Phys Rev B* *76*, 045302. 10.1103/PhysRevB.76.045302.
- [8] Fu, L., and Kane, C.L. (2008). Superconducting proximity effect and majorana fermions at the surface of a topological insulator. *Phys Rev Lett* *100*, 096407. 10.1103/PhysRevLett.100.096407.
- [9] Fu, L., Kane, C.L., and Mele, E.J. (2007). Topological insulators in three dimensions. *Phys Rev Lett* *98*, 106803. 10.1103/PhysRevLett.98.106803.
- [10] Gao, B., Gao, P., Lu, S., Lv, J., Wang, Y., and Ma, Y. (2019). Interface structure prediction via CALYPSO method. *Sci Bull* *64*, 301. 10.1016/j.scib.2019.02.009.
- [11] Gomis, O., Vilaplana, R., Manjón, F.J., Rodríguez-Hernández, P., Pérez-González, E., Muñoz, A., Kucek, V., and Drasar, C. (2011). Lattice dynamics of Sb₂Te₃ at high pressures. *Phys Rev B* *84*, 174305. 10.1103/PhysRevB.84.174305.
- [12] Gupta, S.N., Singh, A., Pal, K., Chakraborti, B., Muthu, D.V.S., Waghmare, U.V., and Sood, A.K. (2017). Raman anomalies as signatures of pressure induced electronic topological and structural transitions in black phosphorus: Experiments and theory. *Phys Rev B* *96*, 094104. 10.1103/PhysRevB.96.094104.
- [13] Hamann, D.R. (2013). Optimized norm-conserving Vanderbilt pseudopotentials. *Phys Rev B* *88*, 085117. 10.1103/PhysRevB.88.085117.
- [14] Hammersley, A.P., Svensson, S.O., Hanfland, M., Fitch, A.N., and Hausermann, D. (1996). Two-dimensional detector software: From real detector to idealised image or two-theta scan. *High Press Res* *14*, 235. 10.1080/08957959608201408.
- [15] Hasan, M.Z., and Kane, C.L. (2010). Colloquium: topological insulators. *Rev Mod Phys* *82*, 3045. 10.1103/RevModPhys.82.3045.
- [16] Hein, R.A., and Swiggard, E.M. (1970). Superconductivity in TlBiTe₂: a low carrier density (III-V)VI₂ compound. *Phys Rev Lett* *24*, 53. 10.1103/PhysRevLett.24.53.
- [17] Jia, W., Cao, Z., Wang, L., Fu, J., Chi, X., Gao, W., and Wang, L.-W. (2013). The analysis of a plane wave pseudopotential density functional theory code on a GPU machine. *Comput Phys Commun* *184*, 9. <https://doi.org/10.1016/j.cpc.2012.08.002>.
- [18] Jia, W., Fu, J., Cao, Z., Wang, L., Chi, X., Gao, W., and Wang, L.-W. (2013). Fast plane wave density functional theory molecular dynamics calculations on multi-GPU machines. *Journal of Computational Physics* *251*, 102. <https://doi.org/10.1016/j.jcp.2013.05.005>.
- [19] Kang, D., Zhou, Y., Yi, W., Yang, C., Guo, J., Shi, Y., Zhang, S., Wang, Z., Zhang, C., Jiang, S., *et al.* (2015). Superconductivity emerging from a suppressed large magnetoresistant state in tungsten ditelluride. *Nat Commun* *6*, 7804.

10.1038/ncomms8804.

[20]Kresse, G., and Furthmüller, J. (1996). Efficiency of ab-initio total energy calculations for metals and semiconductors using a plane-wave basis set. *Comput Mater Sci* 6, 15. 10.1016/0927-0256(96)00008-0.

[21]Kresse, G., and Furthmüller, J. (1996). Efficient iterative schemes for ab initio total-energy calculations using a plane-wave basis set. *Phys Rev B* 54, 11169. 10.1103/PhysRevB.54.11169.

[22]Kresse, G., and Joubert, D. (1999). From ultrasoft pseudopotentials to the projector augmented-wave method. *Phys Rev B* 59, 1758. 10.1103/PhysRevB.59.1758.

[23]Kuroda, K., Eguchi, G., Shirai, K., Shiraishi, M., Ye, M., Miyamoto, K., Okuda, T., Ueda, S., Arita, M., Namatame, H., *et al.* (2015). Tunable spin current due to bulk insulating property in the topological insulator $\text{Tl}_{1-x}\text{Bi}_{1+x}\text{Se}_{2-\delta}$. *Phys Rev B* 91, 205306. 10.1103/PhysRevB.91.205306.

[24]Kuroda, K., Ye, M., Schwier, E.F., Nurmamat, M., Shirai, K., Nakatake, M., Ueda, S., Miyamoto, K., Okuda, T., Namatame, H., *et al.* (2013). Experimental verification of the surface termination in the topological insulator TlBiSe_2 using core-level photoelectron spectroscopy and scanning tunneling microscopy. *Phys Rev B* 88, 245308. 10.1103/PhysRevB.88.245308.

[25]Laroche, D., Bouman, D., van Woerkom, D.J., Proutski, A., Murthy, C., Pikulin, D.I., Nayak, C., van Gulik, R.J.J., Nygard, J., Krogstrup, P., *et al.* (2019). Observation of the 4π -periodic Josephson effect in indium arsenide nanowires. *Nat Commun* 10, 245. 10.1038/s41467-018-08161-2.

[26]Larson, A.C., and Dreele, R.B.V. (2004). General structure analysis system (GSAS). Los Alamos National Laboratory Report LAUR 86.

[27]Mao, H.K., Xu, J., and Bell, P.M. (1986). Calibration of the ruby pressure gauge to 800 kbar under quasi-hydrostatic conditions. *J Geophys Res* 91, 4673. 10.1029/JB091iB05p04673.

[28]Moore, J.E. (2010). The birth of topological insulators. *Nature* 464, 194. 10.1038/nature08916.

[29]Mostofi, A.A., Yates, J.R., Lee, Y.-S., Souza, I., Vanderbilt, D., and Marzari, N. (2008). wannier90: A tool for obtaining maximally-localised Wannier functions. *Computer Physics Communications* 178, 685-699. 10.1016/j.cpc.2007.11.016.

[30]Neupane, M., Xu, S.Y., Sankar, R., Alidoust, N., Bian, G., Liu, C., Belopolski, I., Chang, T.R., Jeng, H.T., Lin, H., *et al.* (2014). Observation of a three-dimensional topological Dirac semimetal phase in high-mobility Cd_3As_2 . *Nat Commun* 5, 3786. 10.1038/ncomms4786.

[31]Novak, M., Sasaki, S., Segawa, K., and Ando, Y. (2015). Large linear magnetoresistance in the Dirac semimetal TlBiSSe . *Phys Rev B* 91, 041203. 10.1103/PhysRevB.91.041203.

[32]Pan, X.C., Chen, X., Liu, H., Feng, Y., Wei, Z., Zhou, Y., Chi, Z., Pi, L., Yen, F., Song, F., *et al.* (2015). Pressure-driven dome-shaped superconductivity and electronic structural evolution in tungsten ditelluride. *Nat Commun* 6, 7805. 10.1038/ncomms8805.

[33]Parlinski, K., Li, Z.Q., and Kawazoe, Y. (1997). First-Principles Determination of

- the Soft Mode in Cubic ZrO_2 . *Phys Rev Lett* 78, 4063. 10.1103/PhysRevLett.78.4063.
- [34]Pei, C., Ying, T., Zhang, Q., Wu, X., Yu, T., Zhao, Y., Gao, L., Li, C., Cao, W., Zhang, Q., *et al.* (2022). Caging-pnictogen-induced superconductivity in skutterudites IrX_3 ($X = \text{As, P}$). *J Am Chem Soc* 144, 6208-6214. 10.1021/jacs.1c09244.
- [35]Pei, C., Ying, T., Zhao, Y., Gao, L., Cao, W., Li, C., Hosono, H., and Qi, Y. (2022). Pressure-induced reemergence of superconductivity in $\mathrm{BaIr}_2\mathrm{Ge}_7$ and $\mathrm{Ba}_3\mathrm{Ir}_4\mathrm{Ge}_{16}$ with cage structures. *Matter Radiat at Extremes* 7, 038404. 10.1063/5.0088235.
- [36]Pei, C., Zhang, J., Wang, Q., Zhao, Y., Gao, L., Gong, C., Tian, S., Luo, R., Lu, Z.-Y., Lei, H., *et al.* (2021). Pressure induced superconductivity at 32 K in MoB_2 . *arXiv:2105.13250*.
- [37]Perdew, J.P., Burke, K., and Ernzerhof, M. (1996). Generalized gradient approximation made simple. *Phys Rev Lett* 77, 3865. 10.1103/PhysRevLett.77.3865.
- [38]Pielmeier, F., Landolt, G., Slomski, B., Muff, S., Berwanger, J., Eich, A., Khajetoorians, A.A., Wiebe, J., Aliev, Z.S., Babanly, M.B., *et al.* (2015). Response of the topological surface state to surface disorder in TlBiSe_2 . *New J Phys* 17, 023067. 10.1088/1367-2630/17/2/023067.
- [39]Ponosov, Y.S., Kuznetsova, T.V., Tereshchenko, O.E., Kokh, K.A., and Chulkov, E.V. (2014). Dynamics of the BiTeI lattice at high pressures. *JETP Lett* 98, 557. 10.1134/s0021364013220074.
- [40]Qi, X.-L., and Zhang, S.-C. (2010). The quantum spin Hall effect and topological insulators. *Phys Today* 63, 33. 10.1063/1.3293411.
- [41]Qi, X.-L., and Zhang, S.-C. (2011). Topological insulators and superconductors. *Rev Mod Phys* 83, 1057. 10.1103/RevModPhys.83.1057.
- [42]Qi, Y., Shi, W., Naumov, P.G., Kumar, N., Sankar, R., Schnelle, W., Shekhar, C., Chou, F.C., Felser, C., Yan, B., *et al.* (2017). Topological quantum phase transition and superconductivity induced by pressure in the bismuth tellurohalide BiTeI . *Adv Mater* 29, 1605965. 10.1002/adma.201605965.
- [43]Sato, T., Segawa, K., Guo, H., Sugawara, K., Souma, S., Takahashi, T., and Ando, Y. (2010). Direct evidence for the dirac-cone topological surface states in the ternary chalcogenide TlBiSe_2 . *Phys Rev Lett* 105, 136802. 10.1103/PhysRevLett.105.136802.
- [44]Sato, T., Segawa, K., Kosaka, K., Souma, S., Nakayama, K., Eto, K., Minami, T., Ando, Y., and Takahashi, T. (2011). Unexpected mass acquisition of Dirac fermions at the quantum phase transition of a topological insulator. *Nat Phys* 7, 840. 10.1038/nphys2058.
- [45]Schlipf, M., and Gygi, F. (2015). Optimization algorithm for the generation of ONCV pseudopotentials. *Comput Phys Commun* 196, 36. <https://doi.org/10.1016/j.cpc.2015.05.011>.
- [46]Souma, S., Komatsu, M., Nomura, M., Sato, T., Takayama, A., Takahashi, T., Eto, K., Segawa, K., and Ando, Y. (2012). Spin polarization of gapped Dirac surface states near the topological phase transition in $\mathrm{TlBi}(\mathrm{S}_{1-x}\mathrm{Se}_x)_2$. *Phys Rev Lett* 109, 186804. 10.1103/PhysRevLett.109.186804.
- [47]Toby, B. (2001). EXPGUI, a graphical user interface for GSAS. *J Appl Crystallogr* 34, 210. 10.1107/S0021889801002242.

- [48]Togo, A., Oba, F., and Tanaka, I. (2008). First-principles calculations of the ferroelastic transition between rutile-type and CaCl_2 -type SiO_2 at high pressures. *Phys Rev B* 78, 134106. 10.1103/PhysRevB.78.134106.
- [49]Vergniory, M.G., Elcoro, L., Felser, C., Regnault, N., Bernevig, B.A., and Wang, Z. (2019). A complete catalogue of high-quality topological materials. *Nature* 566, 480-485. 10.1038/s41586-019-0954-4.
- [50]Wang, Y., Lv, J., Zhu, L., and Ma, Y. (2010). Crystal structure prediction via particle-swarm optimization. *Phys Rev B* 82, 094116. 10.1103/PhysRevB.82.094116.
- [51]Wang, Y., Lv, J., Zhu, L., and Ma, Y. (2012). CALYPSO: A method for crystal structure prediction. *Comput Phys Commun* 183, 2063-2070. 10.1016/j.cpc.2012.05.008.
- [52]Wang, Z., Segawa, K., Sasaki, S., Taskin, A.A., and Ando, Y. (2015). Ferromagnetism in Cr-doped topological insulator TlSbTe_2 . *APL Mater* 3, 083302. 10.1063/1.4922002.
- [53]Wang, Z., Taskin, A.A., Froelich, T.J., Braden, M., and Ando, Y. (2016). Superconductivity in $\text{Tl}_{0.6}\text{Bi}_2\text{Te}_3$ derived from a topological insulator. *Chem Mater* 28, 779. 10.1021/acs.chemmater.5b03727.
- [54]Wiedenmann, J., Bocquillon, E., Deacon, R.S., Hartinger, S., Herrmann, O., Klapwijk, T.M., Maier, L., Ames, C., Brune, C., Gould, C., *et al.* (2016). 4π -periodic Josephson supercurrent in HgTe-based topological Josephson junctions. *Nat Commun* 7, 10303. 10.1038/ncomms10303.
- [55]Wu, Q., Zhang, S., Song, H.-F., Troyer, M., and Soluyanov, A.A. (2018). WannierTools: An open-source software package for novel topological materials. *Computer Physics Communications* 224, 405-416. 10.1016/j.cpc.2017.09.033.
- [56]Xiao, J., and Yan, B. (2021). First-principles calculations for topological quantum materials. *Nature Reviews Physics* 3, 283. 10.1038/s42254-021-00292-8.
- [57]Xu, S.-Y., Xia, Y., Wray, L.A., Jia, S., Meier, F., Dil, J.H., Osterwalder, J., Slomski, B., Bansil, A., Lin, H., *et al.* (2011). Topological phase transition and texture inversion in a tunable topological insulator. *Science* 332, 560. 10.1126/science.1201607.
- [58]Yan, B., and Felser, C. (2017). Topological Materials: Weyl Semimetals. *Annual Review of Condensed Matter Physics* 8, 337. 10.1146/annurev-conmatphys-031016-025458.
- [59]Yan, B., Liu, C.-X., Zhang, H.-J., Yam, C.-Y., Qi, X.-L., Frauenheim, T., and Zhang, S.-C. (2010). Theoretical prediction of topological insulators in thallium-based III-V-VI₂ ternary chalcogenides. *EPL* 90, 37002. 10.1209/0295-5075/90/37002.
- [60]Zhang, Q., Cheng, Y., and Schwingenschlogl, U. (2015). Emergence of topological and topological crystalline phases in TlBiS_2 and TlSbS_2 . *Sci Rep* 5, 8379. 10.1038/srep08379.

FIGURE TITLES

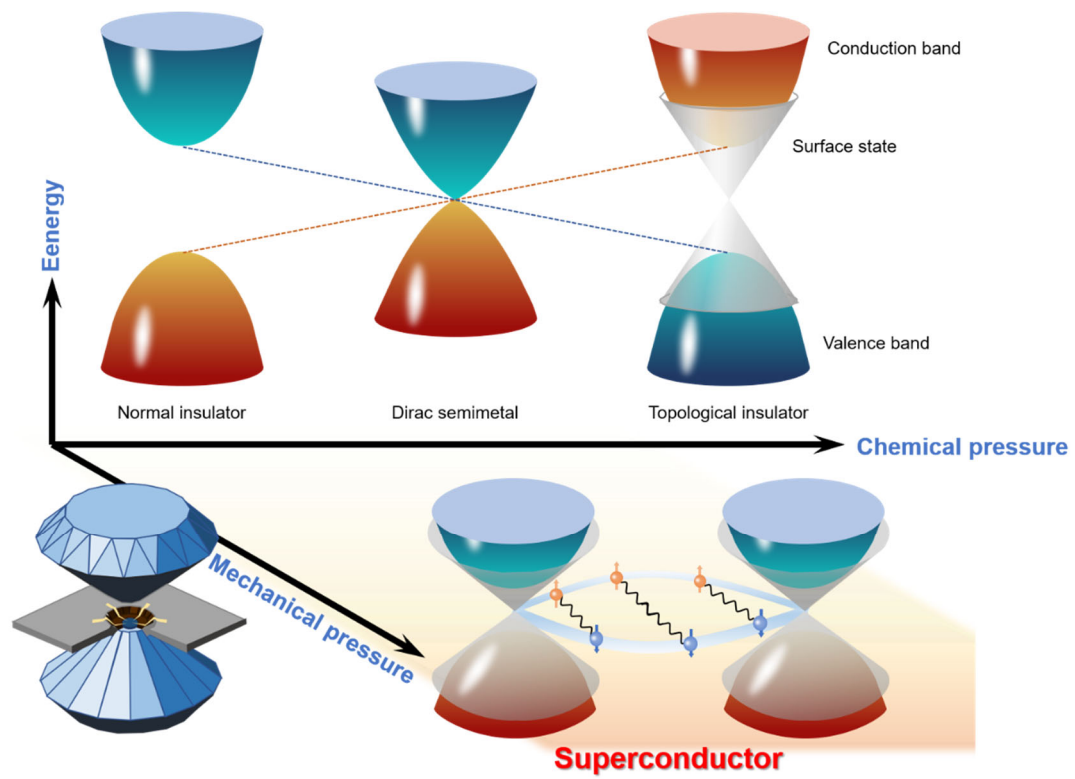


Figure 1. Schematic of chemical pressure and mechanical pressure effect on $\text{TlBi}(\text{S}_{1-x}\text{Se}_x)_2$ compounds.

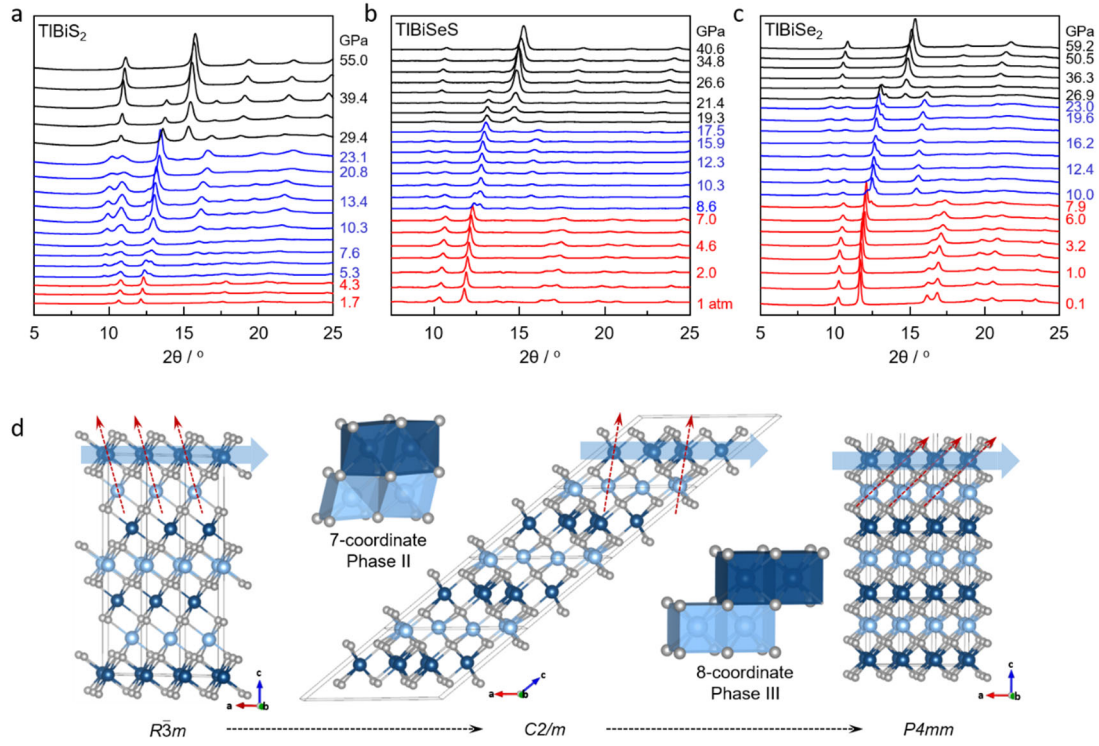


Figure 2. Crystal structure evolution under high pressure. (a) XRD patterns of TlBiSeS under pressure at room temperature with an x-ray wavelength of $\lambda = 0.6199 \text{ \AA}$. The red, blue, and black patterns distinguish phase transition from phase I ($R\bar{3}m$) to phase II ($C2/m$) and phase III ($P4mm$), respectively; (b) Pressure-dependence of volume for TlBiSeS in phase I ($R\bar{3}m$), phase II ($C2/m$), and phase III ($P4mm$); (c) Raman spectra of TlBiSeS under pressure at room temperature; (d) Crystallographic structure of the three phases of TlBiSeS under various pressures.

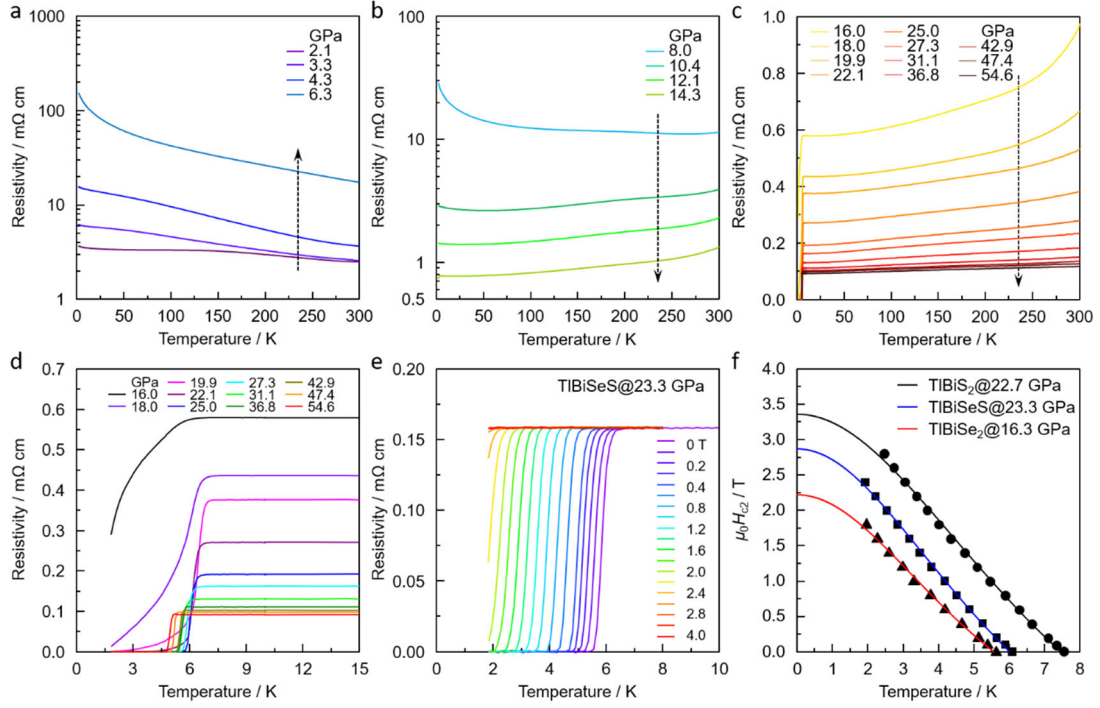


Figure 3. Evolution of the electrical resistivity as a function of pressure. Electrical resistivity of TlBiSeS as a function of temperature for various pressures in run II (a, b, and c); (d) Temperature-dependent resistivity of TlBiSeS in the vicinity of the superconducting transition in run II; (e) Temperature dependence of resistivity under different magnetic fields for TlBiSeS at 23.3 GPa in run III; (f) Temperature dependence of upper critical field for TlBiS₂ at 22.7 GPa, TlBiSeS at 23.3 GPa and TlBiSe₂ at 16.3 GPa, respectively. T_c is determined as the 90% drop of the normal state resistivity. The solid lines represent the Ginzburg–Landau (G-L) fitting. The $\mu_0 H_{c2}(0)$ is 3.36, 2.86, and 2.22 T, respectively.

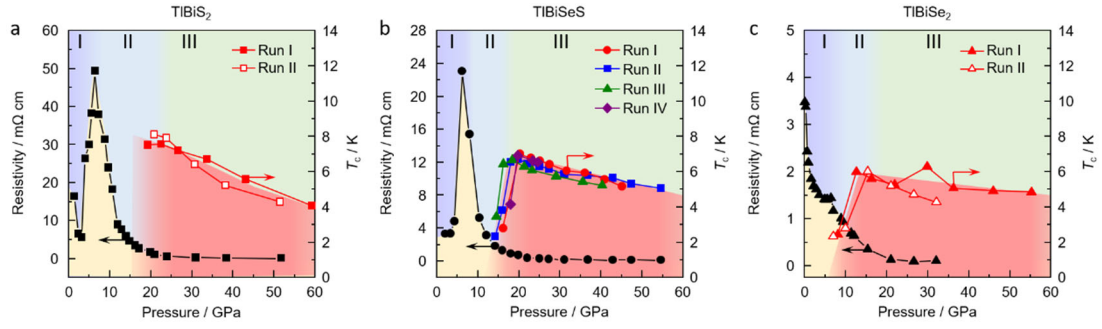


Figure 4. Phase diagram for TlBiS₂, TlBiSeS, and TlBiSe₂. The superconducting T_c and resistivity as a function of pressure at 300 K for TlBiS₂ (a), TlBiSeS (b), and TlBiSe₂ (c) in different runs. The values of T_c onset were determined from the high-pressure resistivity. The purple, blue, and green region stands for phase I ($R\bar{3}m$), phase II ($C2/m$), and phase III ($P4mm$), respectively.

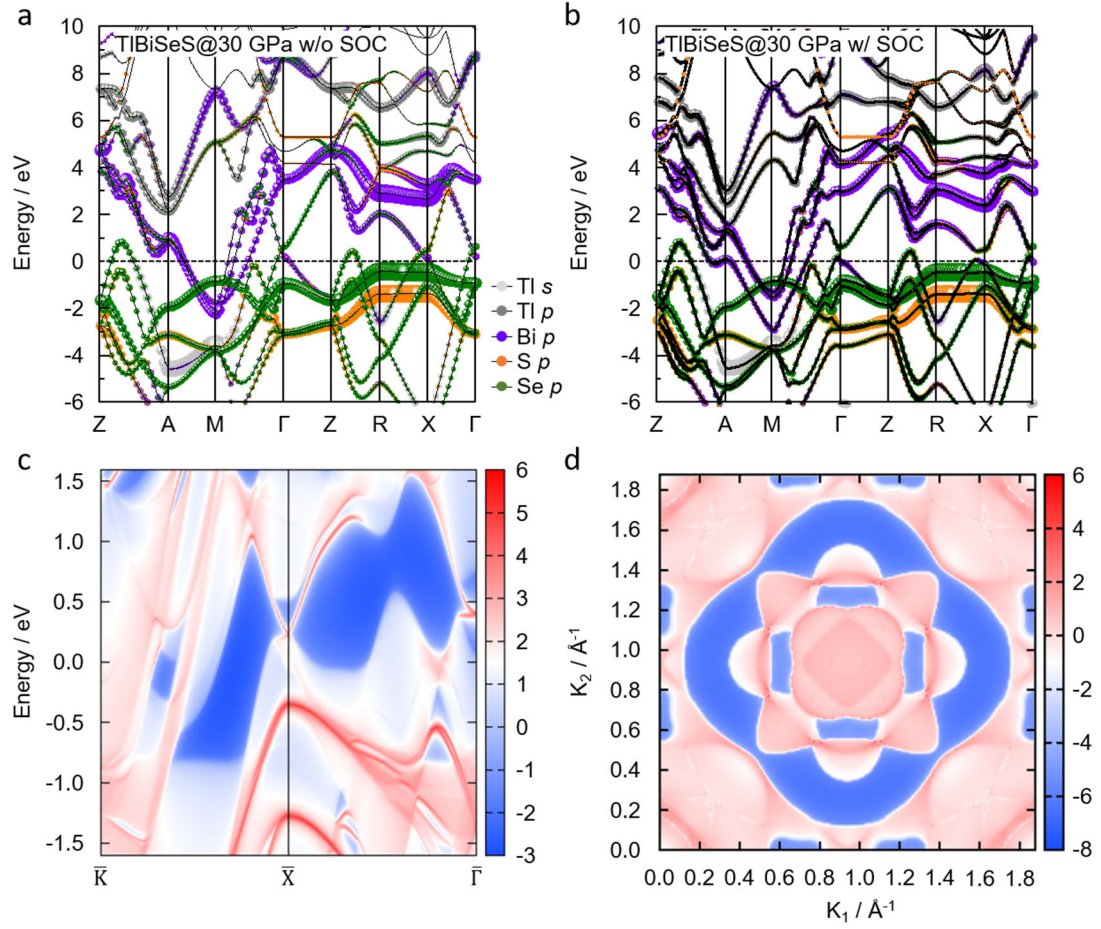


Figure 5. Calculated Fermi surface and band structure under high pressure. Orbital-resolved band dispersions near Fermi level for TlBiSeS at 30 GPa (a) without and (b) with SOC calculated by using PBE; (c) Calculated topological edge states of TlBiSeS with SOC; (d) The (111)-surface Fermi surface of TlBiSeS at $E = 0$ eV.

Supporting Information

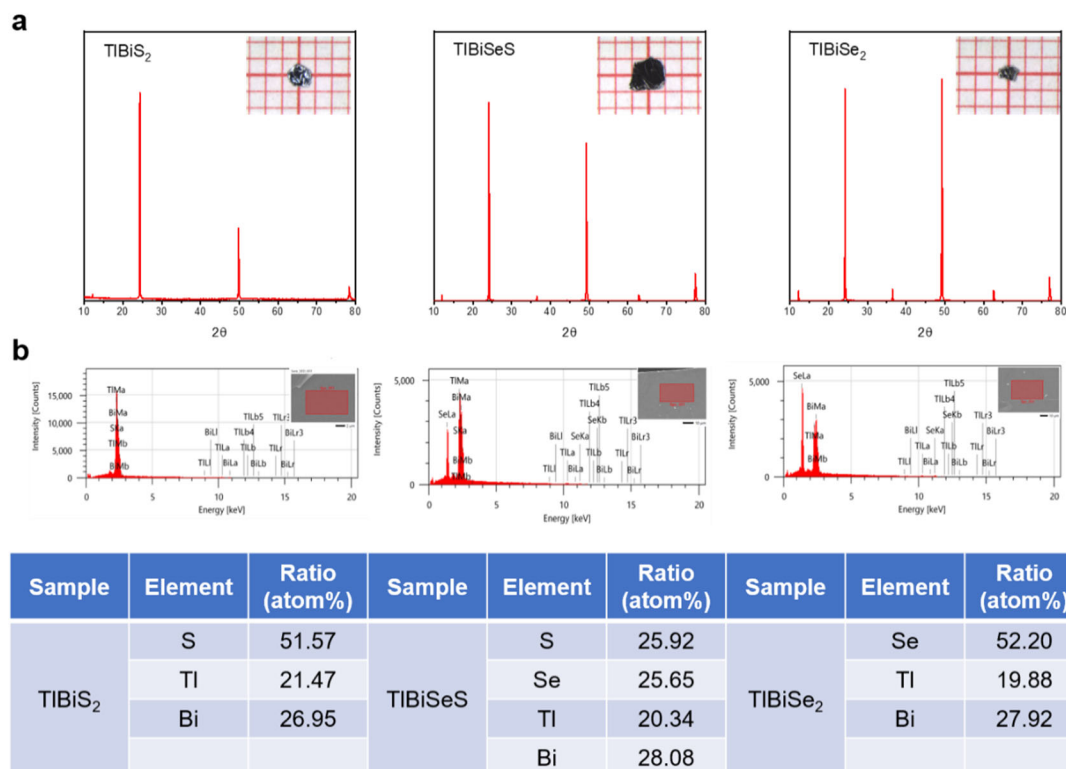


Figure S1. (a) The room temperature powder XRD peaks of TlBiS₂, TlBiSeS and TlBiSe₂ crystal. Insert pictures are the images of typical TlBiS₂, TlBiSeS and TlBiSe₂ single crystal synthesized in this work, respectively; (b) The stoichiometry of TlBiS₂, TlBiSeS and TlBiSe₂ crystal measured by the EDS spectrum. Insert pictures show the crystal used for EDS measurements, respectively. The average compositions derived from a typical EDS measured at several points on the crystal.

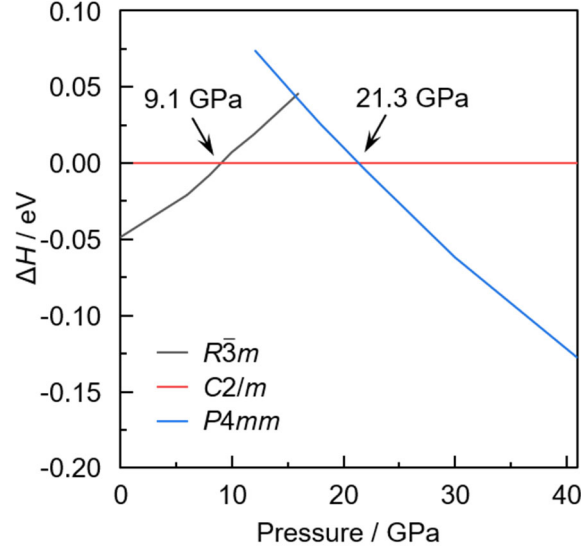


Figure S2. Calculated enthalpies versus pressure of various TlBiSeS structures relative to that of the $C2/m$ phase.

We have examined structures of TlBiSeS by using our developed structure search method^[10; 50; 51]. Structure searches are carried out at 0, 12, 16 and 30 GPa with simulation cells ranging from one to four formula units. Three stable phases were found in the pressure range 0-40 GPa. At 0 GPa, our structure searches simulation successfully reproduced the $R\bar{3}m$ phase, in agreement with previous studies and with the same symmetry as TlBiS₂ and TlBiSe₂. Upon compression, $C2/m$ is found to become more stable than the $R\bar{3}m$ phase at 9.1 GPa. At higher pressure, the $P4mm$ phase is stable above 21.3 GPa.

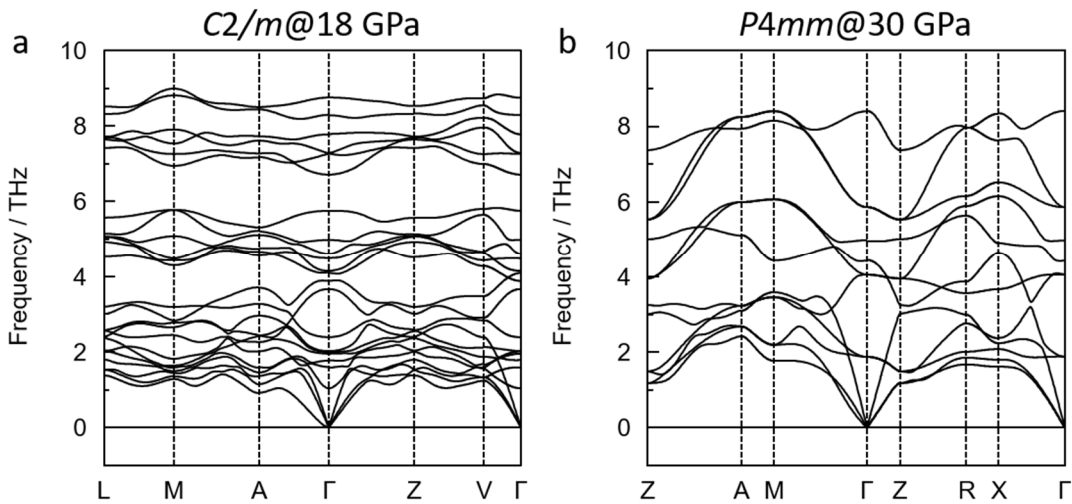


Figure S3. Phonon dispersion of the $C2/m$ -structure TlBiSeS at 18 GPa (a) and $P4mm$ -structure at 30 GPa (b), respectively. No imaginary frequency was found for these two structures, indicating dynamical stability of two high pressure phases of TlBiSeS.

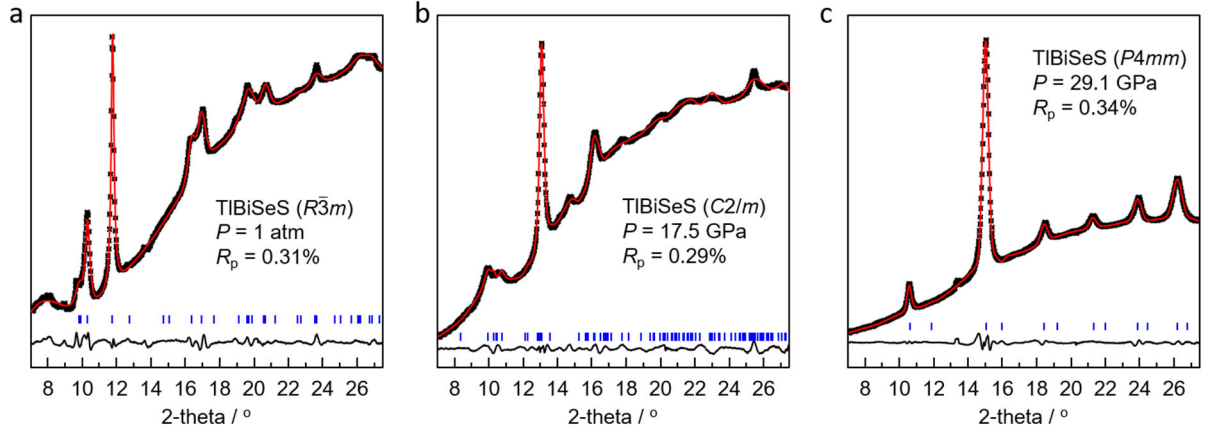


Figure S4. Typical Rietveld refinement results of TlBiSeS under 1 atm (a), 17.5 GPa (b) and 29.1 GPa (c), respectively. The experimental and simulated data were symbolled with black stars and red line. The solid lines shown at the bottom of the figures are the residual intensities. The vertical bars indicate peak positions of the Bragg reflections for TlBiSeS in $R\bar{3}m$ (a), $C2/m$ (b) and $P4mm$ (c) space groups.

Table S1. Structural parameters of the three high pressure phases of TlBiSeS at room temperature.

	phase I	phase II	phase III
Pressure	1 atm	17.5 GPa	29.1 GPa
Crystal system	rhombohedral	monoclinic	tetragonal
Space group	$R\bar{3}m$ (166)	$C2/m$ (12)	$P4mm$ (99)
a	4.205(2)	13.656(1)	3.350(4)
b	4.205(2)	3.783(1)	3.350(4)
c	21.734(1)	10.938(4)	6.698(5)
α	90	90	90
β	90	141.4(1)	90
γ	120	90	90
atoms position	Wyckoff (x y z)	Wyckoff (x y z)	Wyckoff (x y z)
Tl	3a (0,0,0)	4i (0.1180,0.5,0.5076)	1a (0,0,0.0916)
Bi	3b (0,0,0.5)	4i (0.1333,0,0.0157)	1a (0,0,0.6063)
Se	6c (0,0,0.2383)	4i (0.8874,0.5,0.7611)	1b (0.5,0.5,0.8315)
S	6c (0,0,0.2625)	4i (0.3628,0.5,0.2207)	1b (0.5,0.5,0.3551)
Residuals ^a / %	R_{wp} : 0.43% R_p : 0.31%	R_{wp} : 0.37% R_p : 0.29%	R_{wp} : 0.54% R_p : 0.34%

^a R_{wp} and R_p as defined in GSAS^[26]

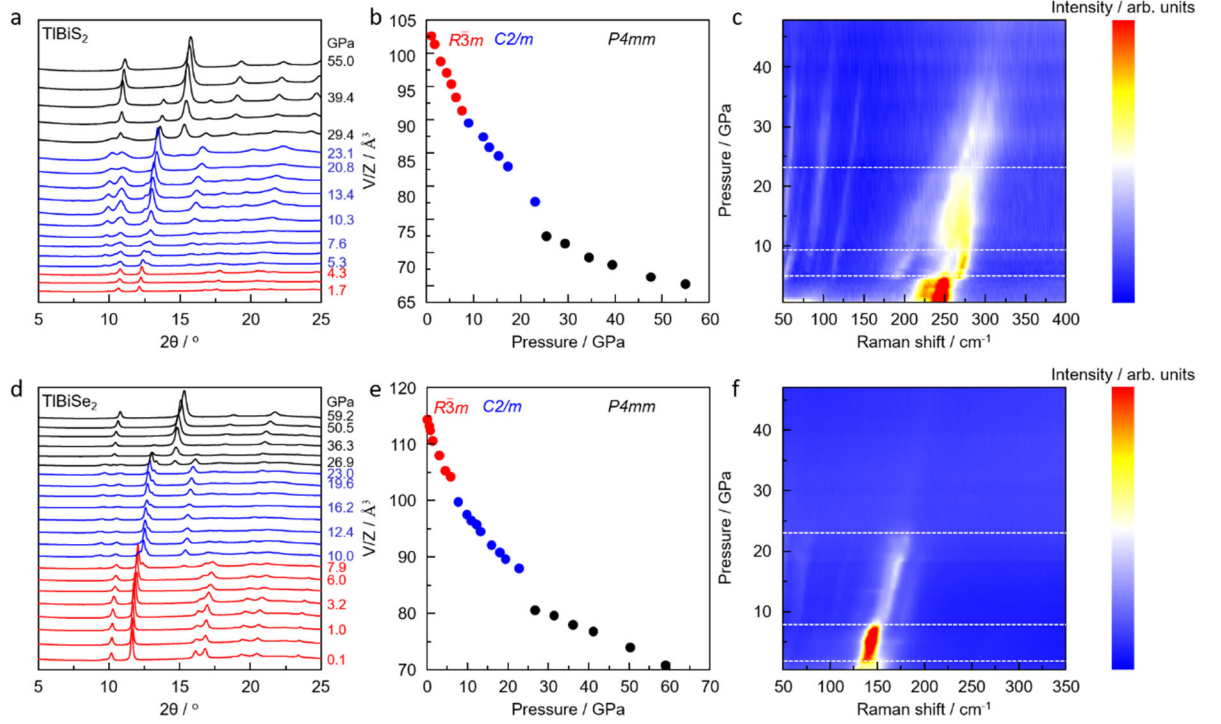


Figure S5. XRD patterns of TlBiS_2 (a) and TlBiSe_2 (d) under pressure at room temperature with an x-ray wavelength of $\lambda = 0.6199 \text{ \AA}$. The red, blue and black patterns distinguish phase transition from phase I ($R\bar{3}m$) to phase II ($C2/m$) and phase III ($P4mm$), respectively; Pressure-dependence of volume for TlBiS_2 (b) and TlBiSe_2 (e) in phase I ($R\bar{3}m$), phase II ($C2/m$) and phase III ($P4mm$); Contour color plot of the pressure-dependent Raman spectra of TlBiS_2 (c) and TlBiSe_2 (f).

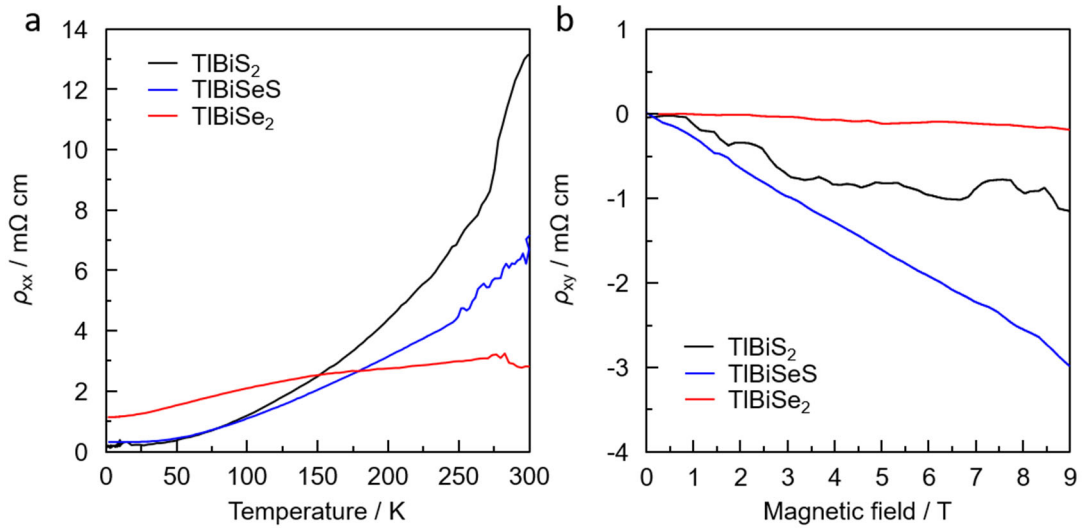


Figure S6. (a) Temperature dependence of the resistivity ρ_{xx} of TlBiS_2 (black), TlBiSeS (blue) and TlBiSe_2 (red) in the absence of a magnetic field, respectively; (b) the field dependence of ρ_{xy} of TlBiS_2 (black), TlBiSeS (blue) and TlBiSe_2 (red) at 300 K, respectively.

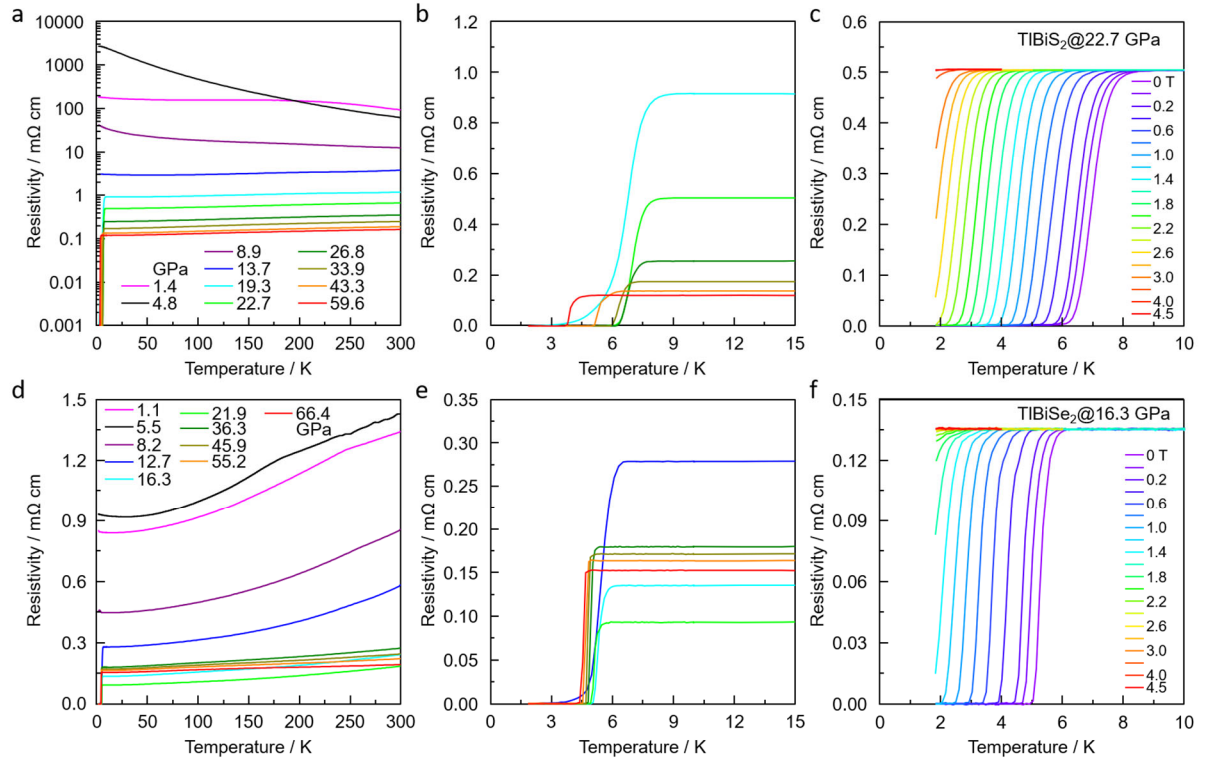


Figure S7. (a) Electrical resistivity of TlBiS₂ as a function of temperature for various pressures in run I; (b) Temperature-dependent resistivity of TlBiS₂ in the vicinity of the superconducting transition; (c) Temperature dependence of resistivity under different magnetic fields for TlBiS₂ at 22.7 GPa; (d) Electrical resistivity of TlBiSe₂ as a function of temperature for various pressures in run I; (e) Temperature-dependent resistivity of TlBiSe₂ in the vicinity of the superconducting transition; (f) Temperature dependence of resistivity under different magnetic fields for TlBiSe₂ at 16.3 GPa.

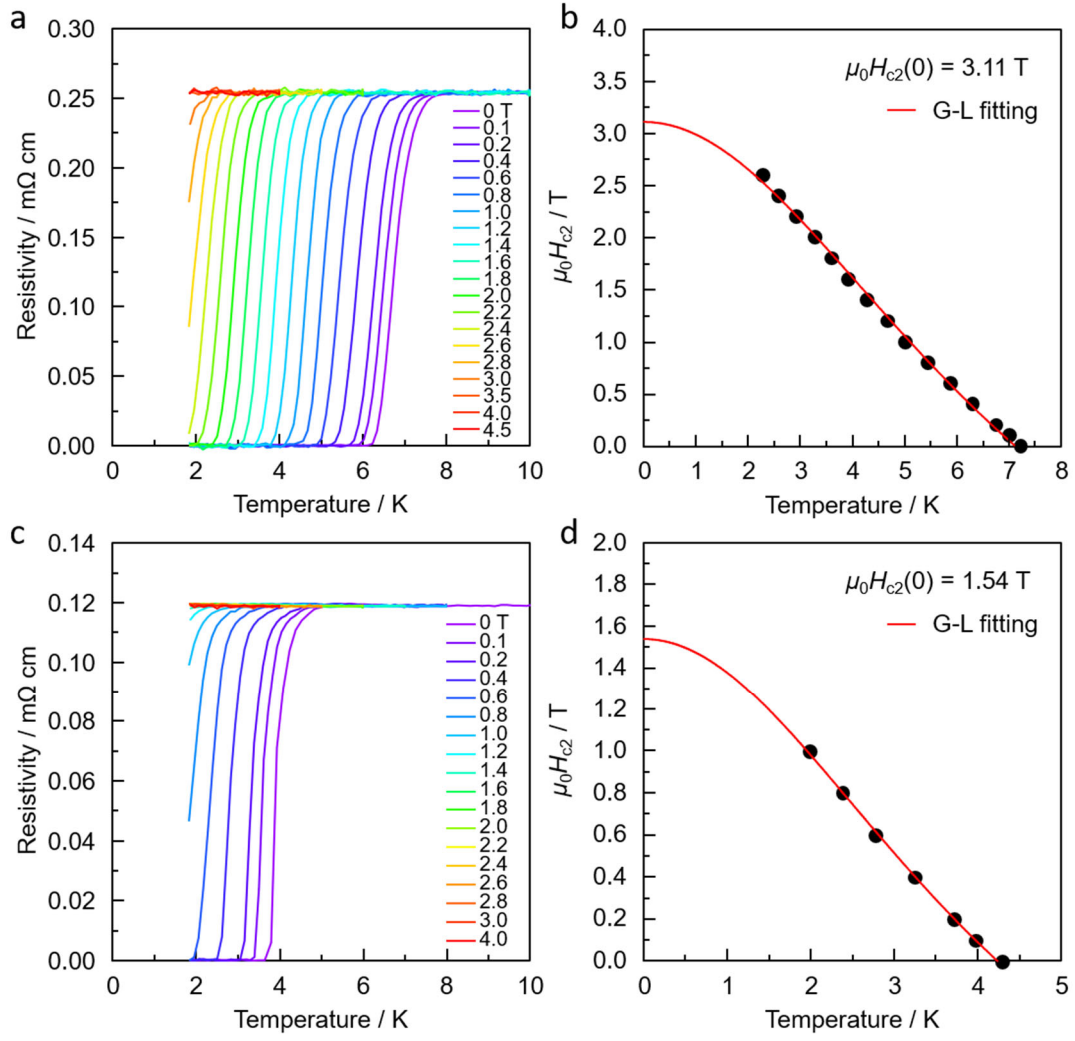


Figure S8. Temperature dependence of resistivity under different magnetic fields for TlBiS₂ at 26.8 GPa (a) and 59.6 GPa (c) in run I; Temperature dependence of upper critical field for TlBiS₂ at 26.8 GPa (a) and 59.6 GPa (c) in run I. Here, T_c is determined as the 90% drop of the normal state resistivity. The solid lines represent the fits based on the Ginzburg–Landau (G-L) formula.

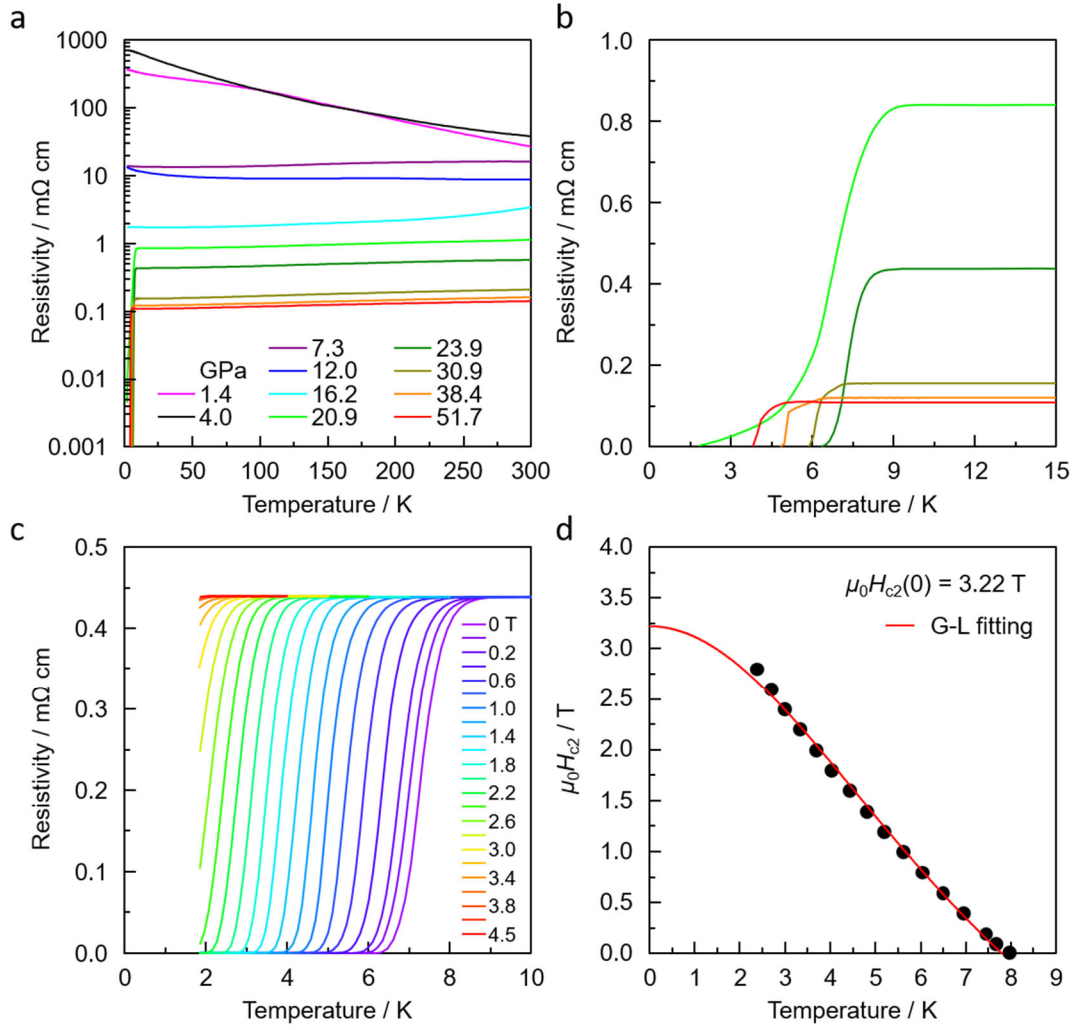


Figure S9. (a) Electrical resistivity of TlBiS₂ as a function of temperature for various pressures in run II; (b) Temperature-dependent resistivity of TlBiS₂ in the vicinity of the superconducting transition in run II; (c) Temperature dependence of resistivity under different magnetic fields for TlBiS₂ at 23.9 GPa; (d) Temperature dependence of upper critical field for TlBiS₂ at 23.9 GPa. Here, T_c is determined as the 90% drop of the normal state resistivity. The solid lines represent the fits based on the Ginzburg–Landau (G-L) formula.

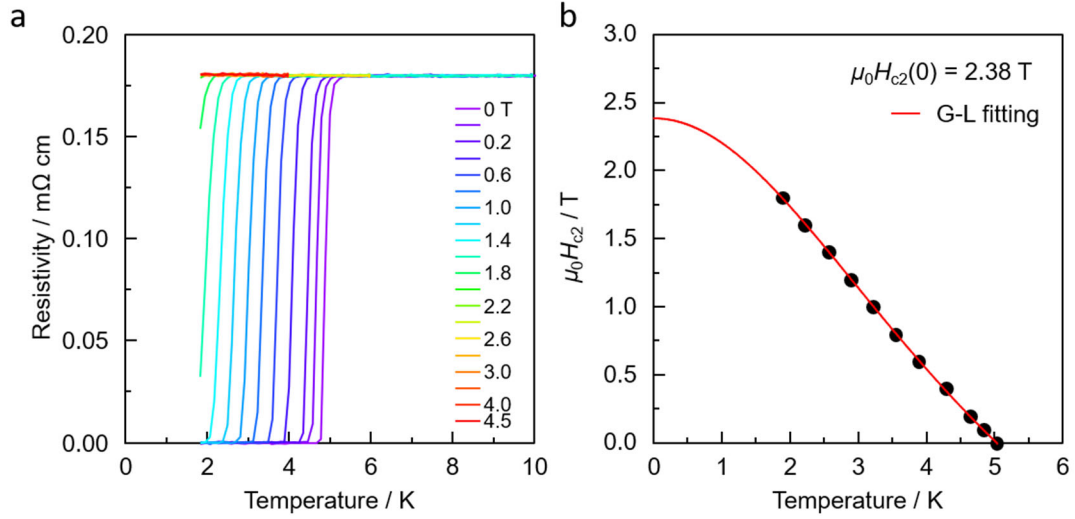


Figure S10. (a) Temperature dependence of resistivity under different magnetic fields for TlBiSe₂ at 36.3 GPa in run I; (b) Temperature dependence of upper critical field for TlBiSe₂ at 36.3 GPa in run I. Here, T_c is determined as the 90% drop of the normal state resistivity. The solid lines represent the fits based on the Ginzburg–Landau (G-L) formula.

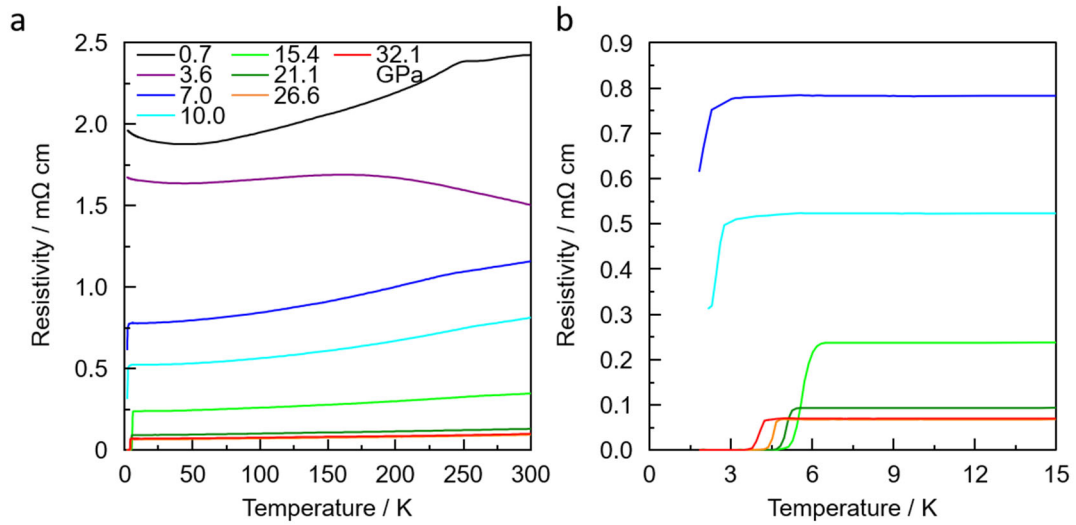


Figure S11. (a) Electrical resistivity of TlBiSe₂ as a function of temperature for various pressures in run II; (b) Temperature-dependent resistivity of TlBiSe₂ in the vicinity of the superconducting transition in run II.

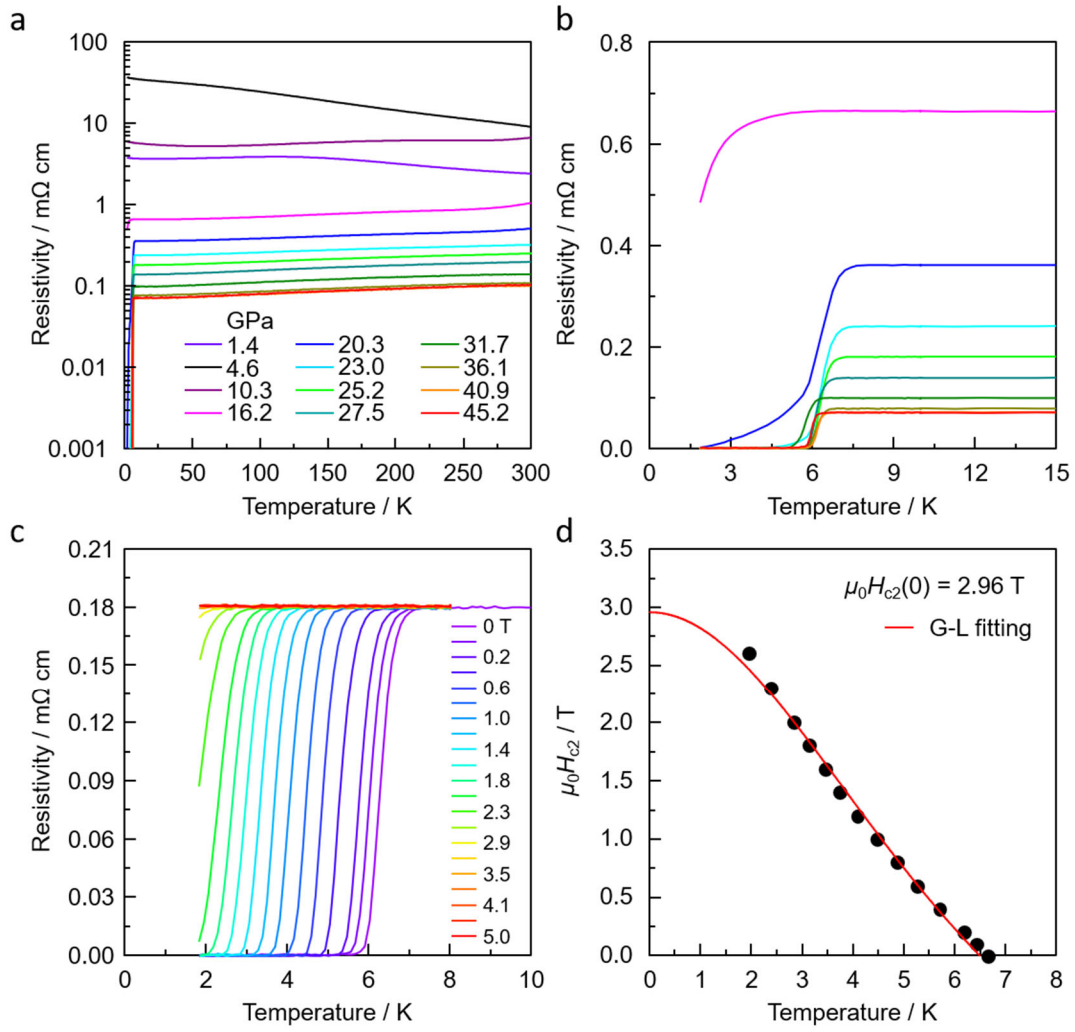


Figure S12. (a) Electrical resistivity of TlBiSeS as a function of temperature for various pressures in run I; (b) Temperature-dependent resistivity of TlBiSeS in the vicinity of the superconducting transition in run I; (c) Temperature dependence of resistivity under different magnetic fields for TlBiSeS at 25.2 GPa; (d) Temperature dependence of upper critical field for TlBiSeS at 25.2 GPa. Here, T_c is determined as the 90% drop of the normal state resistivity. The solid lines represent the fits based on the Ginzburg–Landau (G-L) formula.

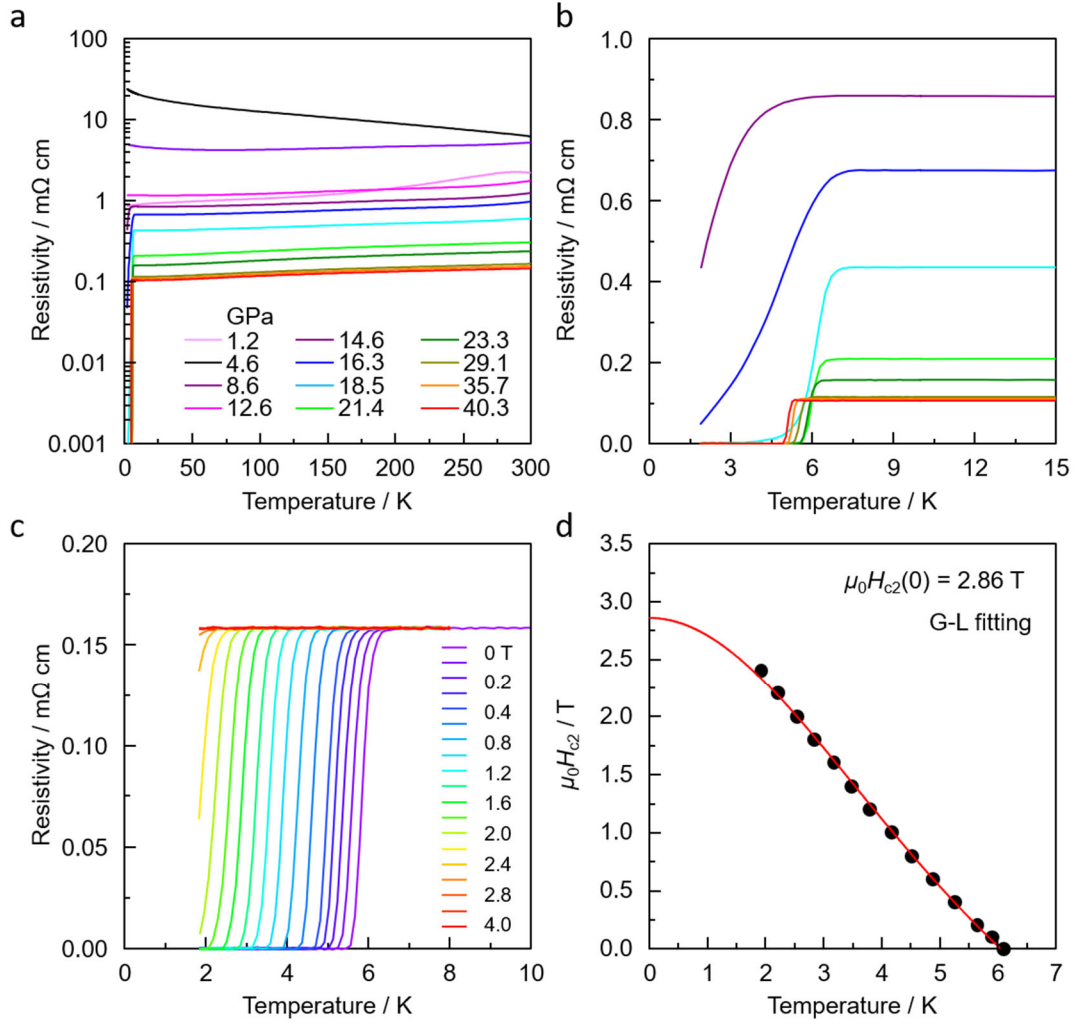


Figure S13. (a) Electrical resistivity of TlBiSeS as a function of temperature for various pressures in run III; (b) Temperature-dependent resistivity of TlBiSeS in the vicinity of the superconducting transition in run III; (c) Temperature dependence of resistivity under different magnetic fields for TlBiSeS at 23.3 GPa; (f) Temperature dependence of upper critical field for TlBiSeS at 23.3 GPa. Here, T_c is determined as the 90% drop of the normal state resistivity.

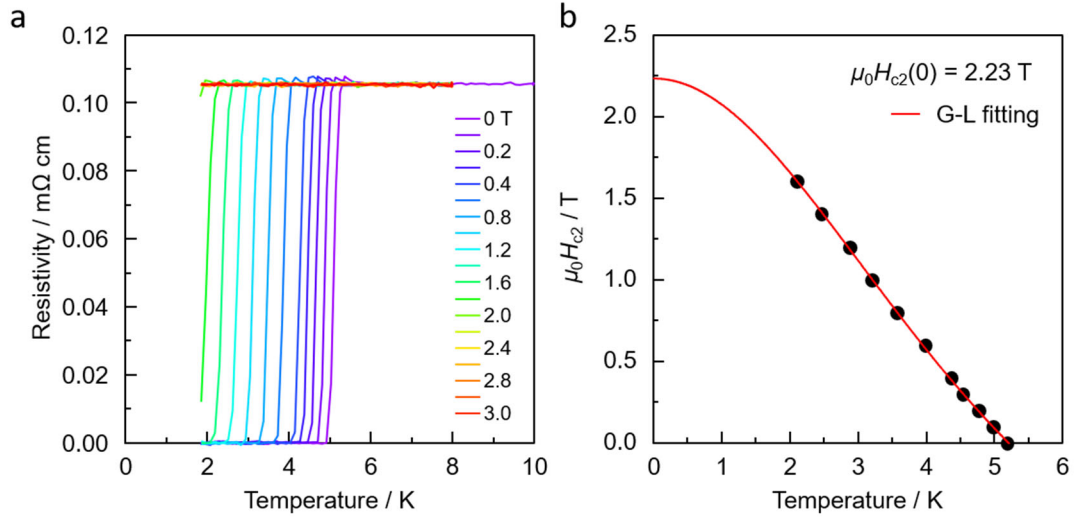


Figure S14. (a) Temperature dependence of resistivity under different magnetic fields for TlBiSeS at 40.3 GPa in run III; (b) Temperature dependence of upper critical field for TlBiSeS at 40.3 GPa in run III. Here, T_c is determined as the 90% drop of the normal state resistivity. The solid lines represent the fits based on the Ginzburg–Landau (G-L) formula.

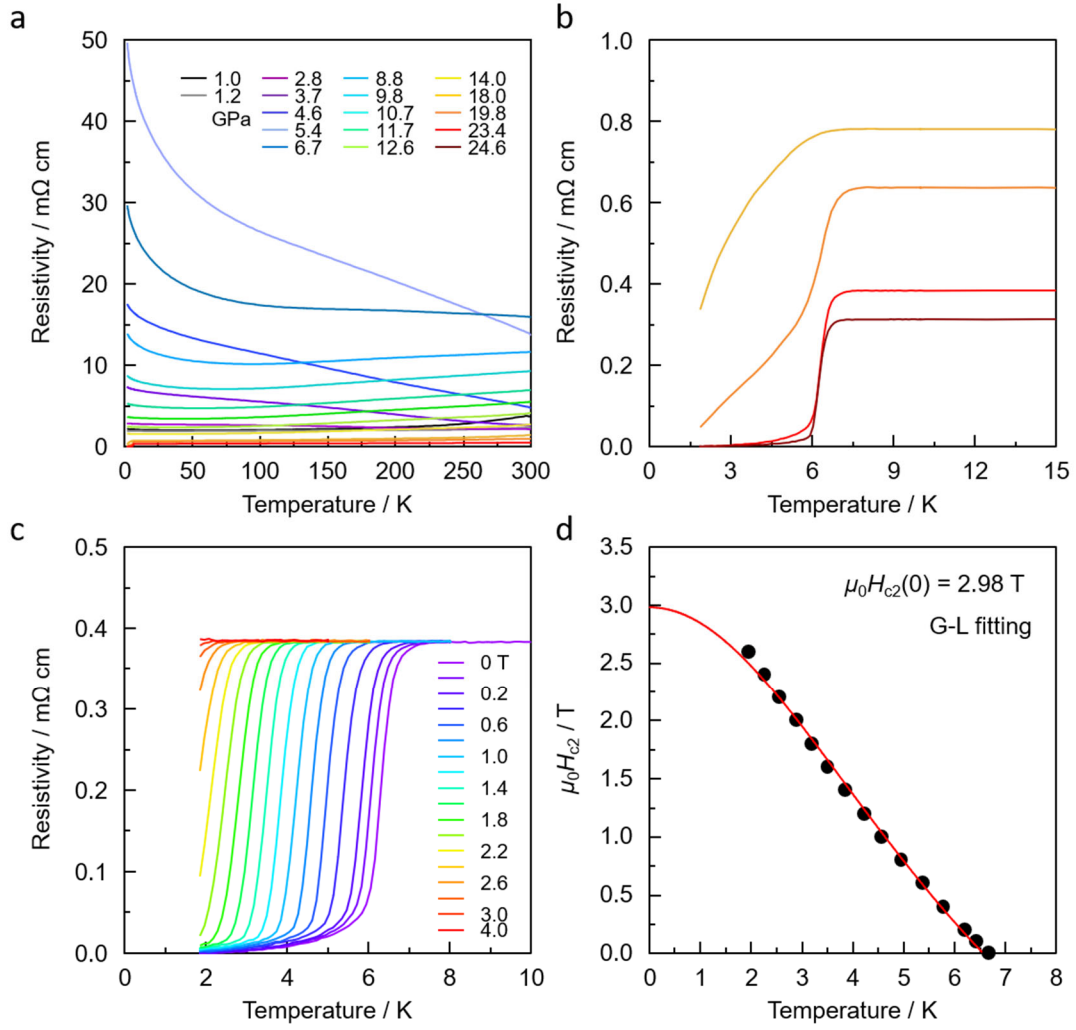


Figure S15. (a) Electrical resistivity of TlBiSeS as a function of temperature for various pressures in run IV; (b) Temperature-dependent resistivity of TlBiSeS in the vicinity of the superconducting transition in run IV; (c) Temperature dependence of resistivity under different magnetic fields for TlBiSeS at 23.4 GPa; (d) Temperature dependence of upper critical field for TlBiSeS at 23.4 GPa. Here, T_c is determined as the 90% drop of the normal state resistivity. The solid lines represent the fits based on the Ginzburg–Landau (G-L) formula.

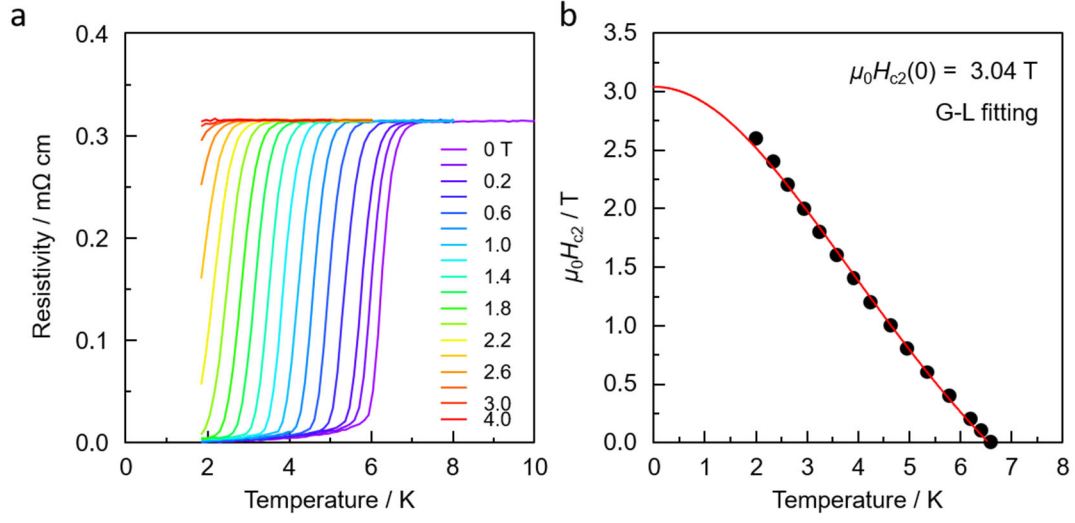


Figure S16. (a) Temperature dependence of resistivity under different magnetic fields for TlBiSeS at 24.64 GPa in run IV; (b) Temperature dependence of upper critical field for TlBiSeS at 24.64 GPa in run IV. Here, T_c is determined as the 90% drop of the normal state resistivity. The solid lines represent the fits based on the Ginzburg–Landau (G-L) formula.

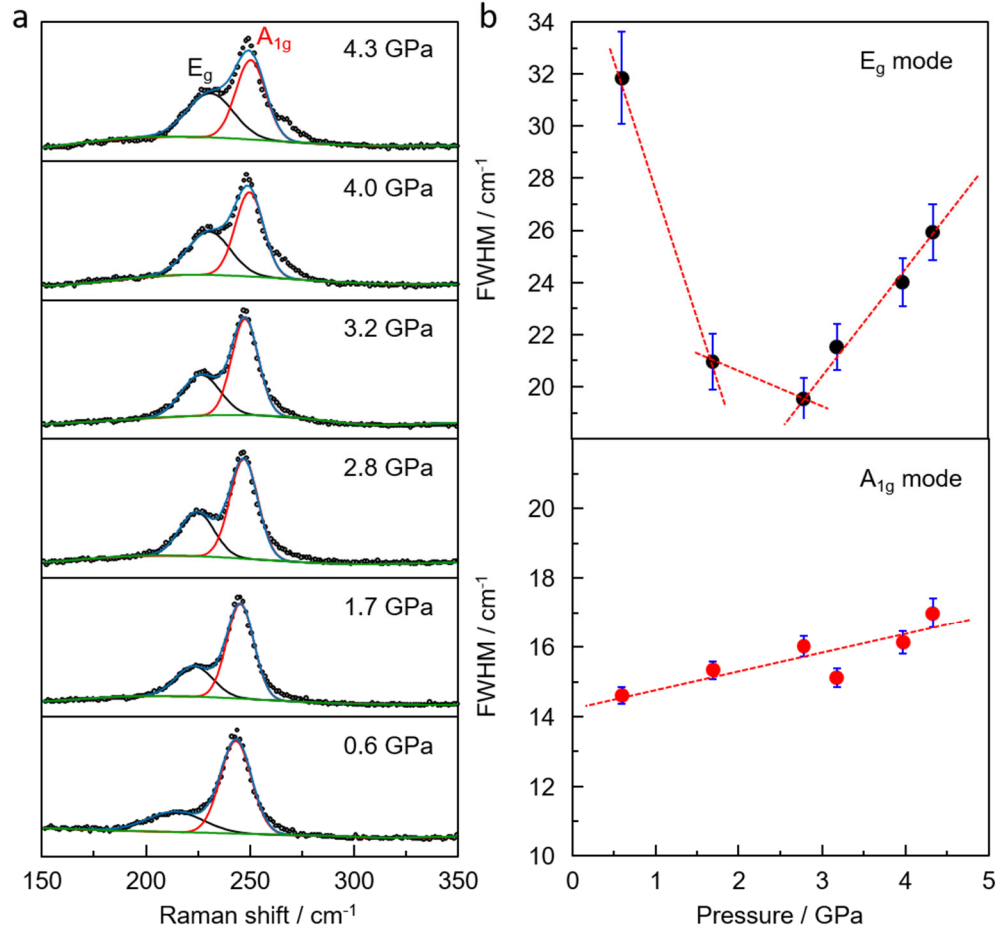


Figure S17. (a) Experimental Raman spectrum of TiBiS₂ at various selected pressures; (b) pressure-dependent of FWHM of E_g and A_{1g} mode. The lines (blue, red, black) are the Gaussian fits to the experimental data (black). Green line stands for the baseline with spline interpolation method.

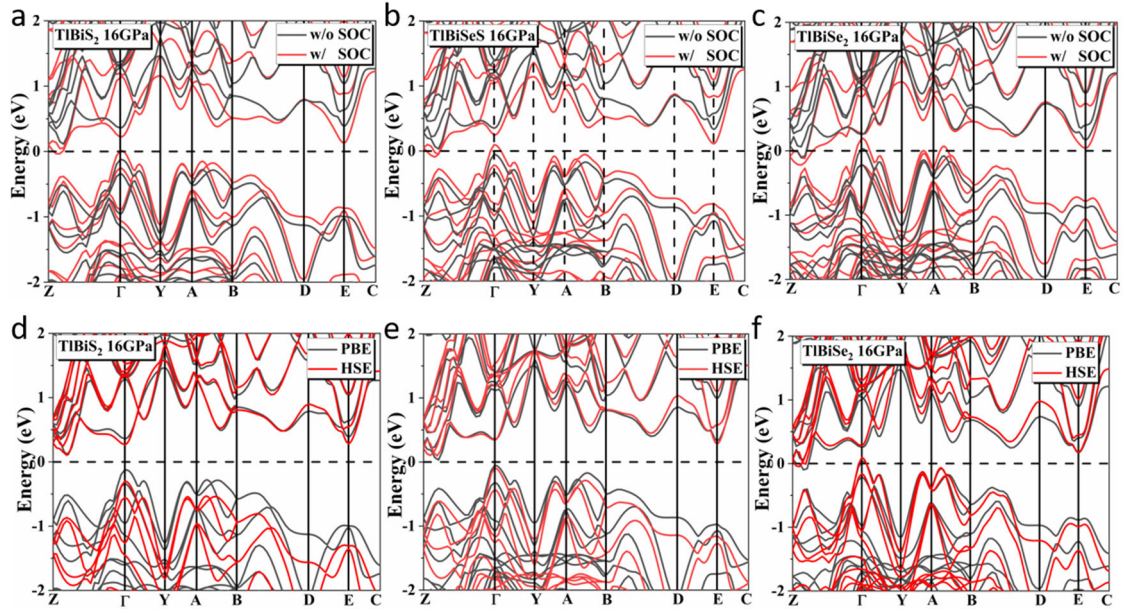
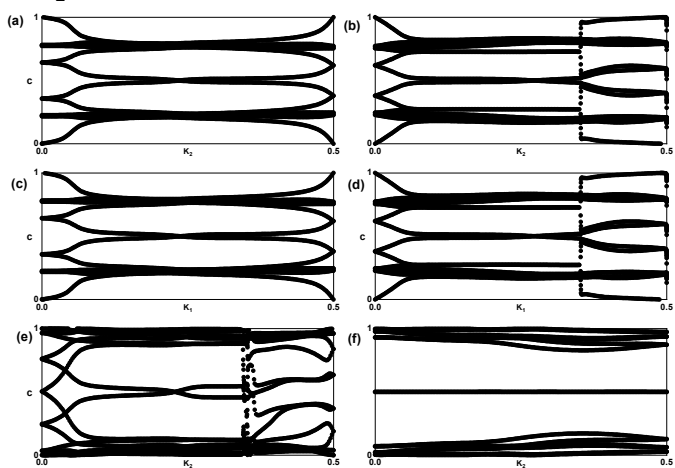
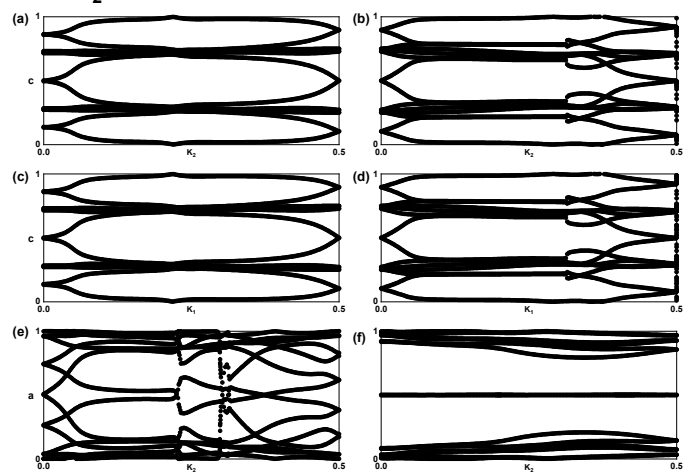


Figure S18. Electronic band structure of TIBiS₂ (a), TIBiSeS (b) and TIBiSe₂ (c) at 16 GPa with/without SOC using the PBE functional; Electronic band structure of TIBiS₂ (d), TIBiSeS (e) and TIBiSe₂ (f) at 16 GPa in absence of SOC using HSE06 Hybrid functional.

TiBiS₂



TiBiSe₂



TiBiSeS

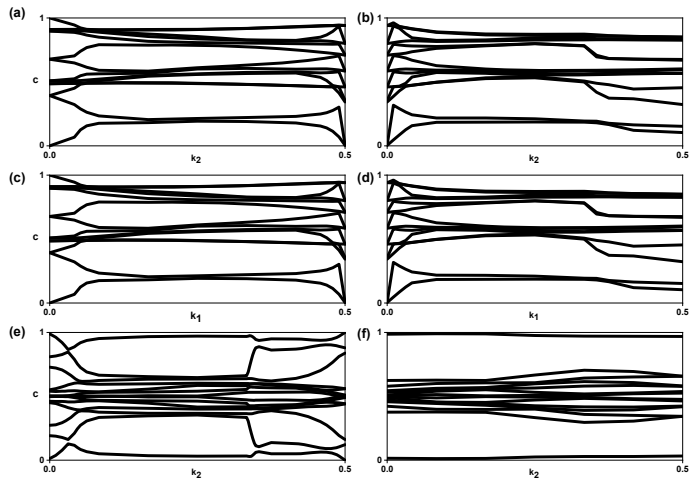


Figure S19. Evolution of Wannier charge centers on six time-reversal invariant momentum planes, (a) $k_1 = 0.0$, (b) $k_1 = 0.5$, (c) $k_2 = 0.0$, (d) $k_2 = 0.5$, (e) $k_3 = 0.0$, and (f) $k_3 = 0.5$ for TiBiS_2 , TiBiSe_2 , and TlBiSeS at 30 GPa.

The Z2 topological invariants for these six planes in TiBiS_2 at 30 GPa are found to be.

$k_1=0.0$, k_2 - k_3 plane:	0
$k_1=0.5$, k_2 - k_3 plane:	0
$k_2=0.0$, k_1 - k_3 plane:	0
$k_2=0.5$, k_1 - k_3 plane:	0
$k_3=0.0$, k_1 - k_2 plane:	1
$k_3=0.5$, k_1 - k_2 plane:	0

The Z2 topological invariants for these six planes in TiBiSe_2 at 30 GPa are found to be.

$k_1=0.0$, k_2 - k_3 plane:	0
$k_1=0.5$, k_2 - k_3 plane:	0
$k_2=0.0$, k_1 - k_3 plane:	0
$k_2=0.5$, k_1 - k_3 plane:	0
$k_3=0.0$, k_1 - k_2 plane:	1
$k_3=0.5$, k_1 - k_2 plane:	0

The Z2 topological invariants for these six planes in TiBiSeS at 30 GPa are found to be.

$k_1=0.0$, k_2 - k_3 plane:	1
$k_1=0.5$, k_2 - k_3 plane:	0
$k_2=0.0$, k_1 - k_3 plane:	1
$k_2=0.5$, k_1 - k_3 plane:	0
$k_3=0.0$, k_1 - k_2 plane:	0
$k_3=0.5$, k_1 - k_2 plane:	0

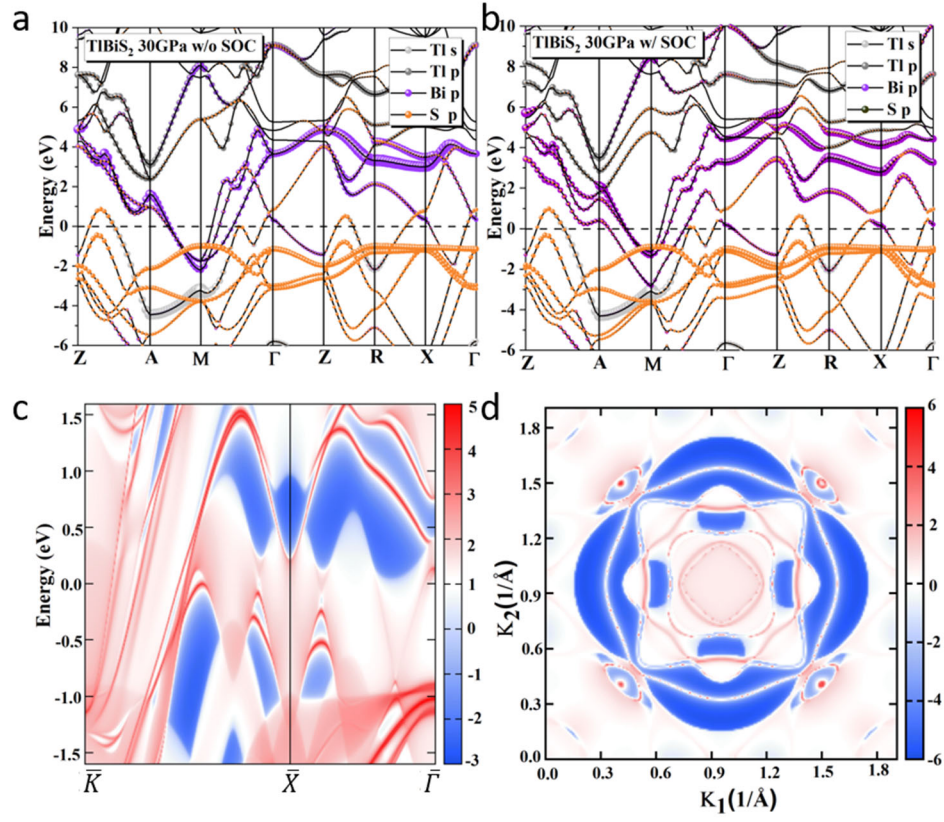


Figure S20. Orbital-resolved band dispersions near Fermi level for TlBiS₂ at 30 GPa (a) without and (b) with SOC calculated by using PBE; (c) Calculated topological edge states of TlBiS₂ with SOC; (d) The (111)-surface Fermi surface of TlBiS₂ at E = 0 eV.

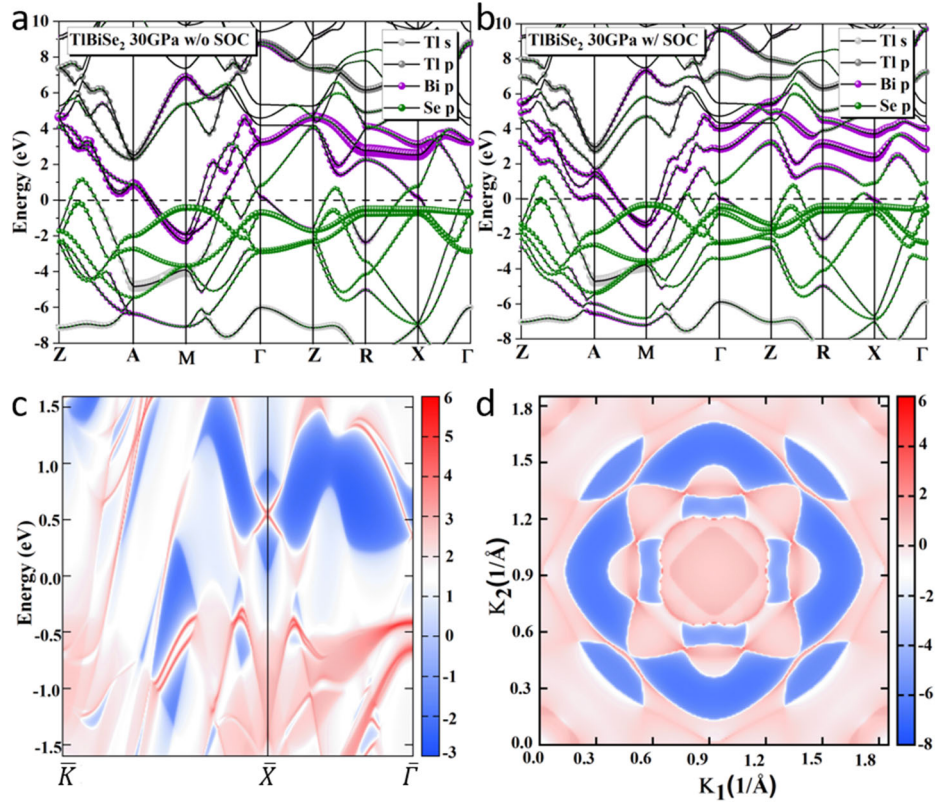


Figure S21. Orbital-resolved band dispersions near Fermi level for TlBiSe₂ at 30 GPa (a) without and (b) with SOC calculated by using PBE; (c) Calculated topological edge states of TlBiSe₂ with SOC; (d) The (111)-surface Fermi surface of TlBiSe₂ at E = 0 eV.

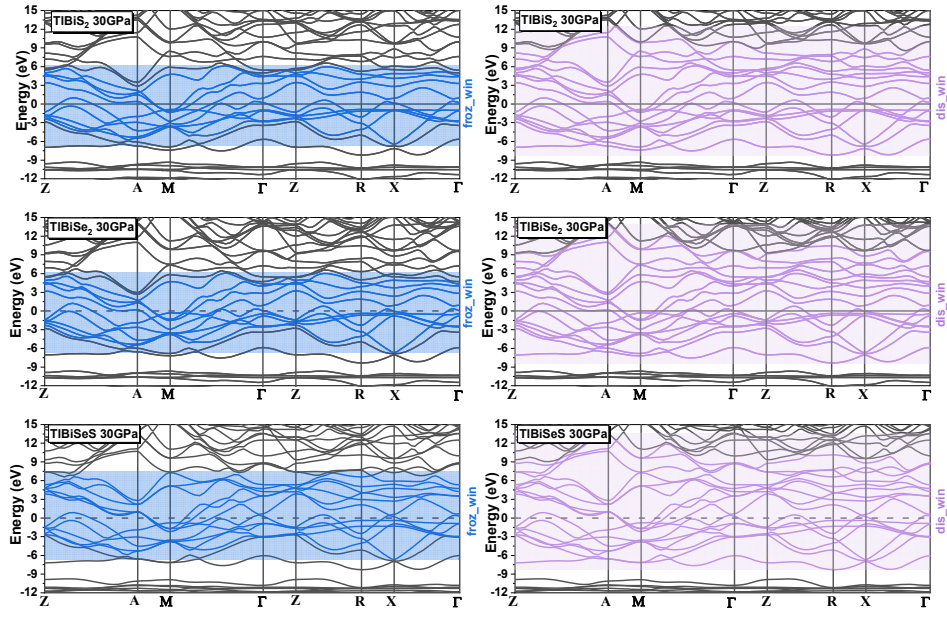


Figure S22. The frozen window `froz_win` (left) and disentanglement window `dis_win` (right) of TiBiS_2 , TiBiSe_2 and TiBiSeS at 30 GPa.

Table S2. The parity of the band at X point for three materials TiBiS_2 , TiBiSe_2 , and TiBiSeS at 30 GPa. Here, we show the parities of twenty occupied bands, and the lowest unoccupied band. The product of the parities for the twenty occupied bands is given in brackets on the right of each row.

	1	2	3	4	5	6	7	8	9	10	11	12	13	14	15	16	17	18	19	20	21	
TiBiS_2	-	-	-	-	-	+	-	-	-	-	-	-	-	-	+	+	-	-	+	+	-	(-)
TiBiSe_2	-	-	-	-	-	+	-	-	-	-	-	-	-	-	+	+	-	-	+	+	-	(-)
TiBiSeS	+	-	+	-	+	-	-	+	+	+	-	+	-	+	-	+	+	-	+	-	+	(-)